

# Chapter 3

## Reservoir Characteristics



### 3.1 Introduction

Organic matter-rich Marine shale is mostly gray-black stone-containing carbon or silica-rich rock phase. Due to the change of reservoir formation environment, plate extrusion and uneven deposition, the thin layered structure is developed, showing obvious anisotropy characteristics. Researchers have studied the hydraulic fracturing characteristics of shale reservoirs based on indoor tests. However, due to the different reservoir formation conditions, shale properties, and stress environment, the hydraulic fracture morphology and fracture propagation law of shale also show obvious anisotropic characteristics. In this chapter, the Longmaxi Formation shale obtained from Sichuan Basin is taken as the research object. The mineral components, the distribution characteristics of pores and fissures, and the mechanical properties of shale are detected and analyzed by means of XRD, nuclear magnetic resonance (NMR), microscope, scanning electron microscope (SEM), and basic mechanical experiments. On this basis, by comparing the indoor hydraulic fracturing tests of Longmaxi shale and Lushan shale, the hydraulic fracturing characteristics of shale reservoirs under different reservoir formation conditions and stress environments are studied.

### 3.2 Sample Preparation

#### 3.2.1 *Sampling Location*

To compare the effects of the Marine sedimentary environment differences on the material properties and fracturing characteristics of shale, the shale specimens obtained from Changning County, Sichuan Province, and the Lushan Mine, Jiangxi Province are taken as test materials (Fig. 3.1). The Longmaxi shale, as the main experimental group, is used to study the hydraulic fracturing characteristics of shale

reservoirs. This kind of shale located at the southern edge of the Sichuan Basin belongs to the Longmaxi Formation of the Silurian system (hereinafter referred to as Longmaxi shale). Affected by the multi-stage tectonic evolution of Changning anticline (deep burial in the early stage, and strong uplift in the later stage) and the deep-water shelf facies sedimentary environment, the Longmaxi shale is characterized by dark mud debris sediment. Its burial depth is generally 2000–4500 m [1, 2], which belongs to the same stratum (about 285 km apart) as Longmaxi Shale in Fuling District, China’s main shale gas production area. The Lushan shale, as a comparison group, is mainly used to analyze the disturbance of the hydraulic fracturing effectiveness caused by the difference of rock properties caused by the reservoir formation environment. This kind of shale with a buried depth of 1000–4000 m [3, 4] belongs to the Upper Sinian of the Lower Paleozoic, mainly located in the Jiujiang depression structural block. Due to the tectonic compression and slippage in the later period, local shale has fragmented silification and decarbonization, but the overall content remains stable, that is, the main component is mainly gray-black siliceous shale.

According to the processing and test procedure shown in Fig. 3.2, the regolith outcrop shale is stripped by mechanical cutting first and then cut off the complete rock block. With reference to the sample specifications and standards of the International Society for Rock Mechanics (ISRM), cylindrical ( $\varphi 50\text{ mm} \times 100\text{ mm}$ ) and cubic ( $200\text{ mm} \times 200\text{ mm}$ ) samples with flatness deviation less than 0.1 mm were prepared by mechanical processing and core drilling sampling methods for uniaxial and true triaxial fracturing tests.

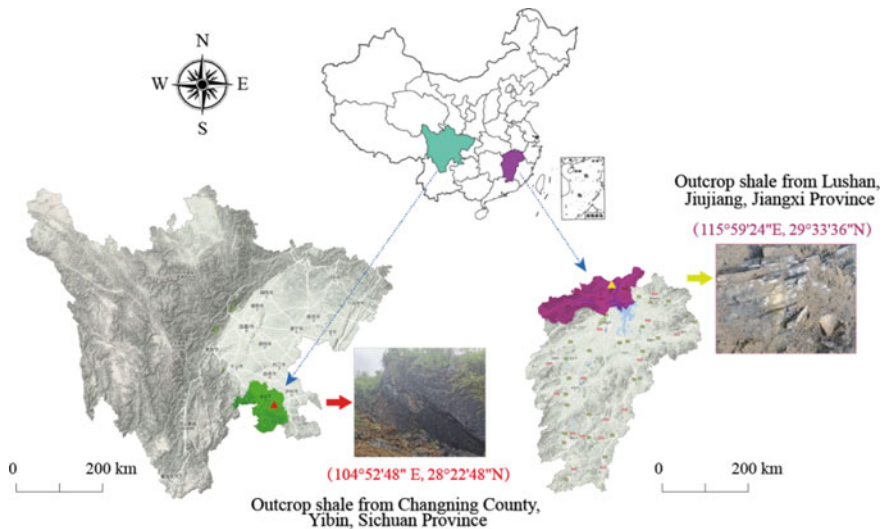


**Fig. 3.1** Schematic diagram of shale sampling location

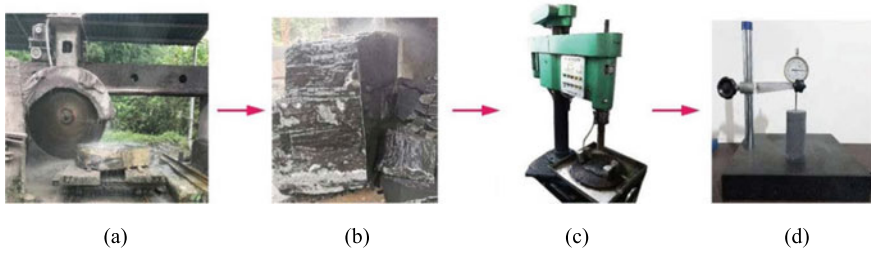


**Fig. 3.2** Processing and preparation of rock samples. **a** Open rock block cutting, **b** complete rock block, **c** drill core sampling, **d** end-surface flatness detection

### 3.2.2 Mineral Composition Characteristics

Small shale pieces were ground to powder with an average particle size of  $\sim 70 \mu\text{m}$ . The Brooke D8 Advanced X-ray diffractometer was used to carry out a conventional XRD diffraction test of shale minerals, with a diffraction angle range of  $5\text{--}90^\circ$  and a scanning rate of  $8^\circ/\text{min}$ . Figure 3.3 shows the X-ray diffraction patterns of two kinds of shale. Based on the whole pattern fitting (WPF) and the Rietveld refined quantitative analysis, the main mineral compositions and relative contents of the two kinds of shale can be determined by using the unique X-ray atlas of each shale component mineral. The relevant results are summarized in Table 3.1.

From Table 3.1, we can see that Longmaxi shale contains 5 types of minerals, mainly quartz and dolomite, where the two types of minerals are similar in content, and the sum is more than 70% of the total content; Lushan shale contains 7 kinds of

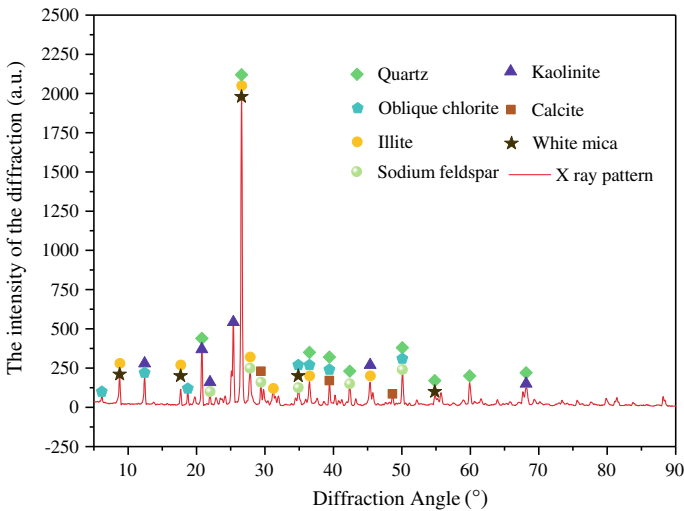


**Fig. 3.3** X-ray diffraction pattern of powder shale sample

**Table 3.1** Summary of relative mineral content of Longmaxi and Lushan shale

Shale	Ingredient					
	Quartz (%)	Albite (%)	Carbonate minerals (%)	Clay mineral (%)	Clinochlore (%)	Talc (%)
Longmaxi Shale	36.3	–	Calcite 15.3 Dolomite 34	Illite 13.7 Kaolinite 0.7	–	–
Lushan shale	25.4	8.7	Calcite 2.5	Illite 40.7 Kaolinite 1	15.1	6.6

minerals, among which illite accounts for the largest proportion, followed by quartz. Compared with the Longmaxi shale, the Lushan shale has a more complex mineral composition, including quartz, carbonate and clay minerals, sodium feldspar, chlorite and dolomite. According to the calculation method of rock mineral brittleness index (the ratio of quartz content to brittle mineral content), the brittleness indexes of the two shales are 36.3 and 36.5, respectively, indicating that the brittleness of the two types of shale is good and their properties are similar and are prone to produce induced fractures during hydraulic fracturing, forming a complex fracturing network. In addition, the content of clay minerals in Lushan shale is 41.7%, which is approximately three times that of Longmaxi shale, which shows that Lushan shale is dominated by clay minerals. The difference in mineral composition and relative content of the two types of shale reflects the difference in their brittleness and sedimentary environments, which ultimately leads to the difference in shale's physical and mechanical properties.

### 3.2.3 Microstructural Characteristics

Shale is a fine-grained sedimentary rock with ultra-low permeability and porosity composed of a matrix, pores, and microcracks. Pores and microcracks are the main places and transmission channels for shale gas free or adsorption and their structure, spatial distribution and connectivity determine the reservoir performance of shale reservoirs. According to the International Federation of Pure and Applied Chemistry (IUPAC) classification standards, shale pores can be divided into micropores, mesopores and macropores on the basis of their pore size (as shown in Fig. 3.4). Microcracks are generally considered that width observed in the perspective of millimeter level is generally less than 1 mm, not limited by the distribution of shale particles, and can be manifested as transgranular crack or intergranular crack [5, 6]. Qualitative description and quantitative characterization of shale microstructural features are important in optimizing hydraulic fracturing design and evaluating reservoir rock properties.

Laboratory visualization of rock microstructural features is mainly achieved by means of CT scanning, microscope observation and scanning electron microscope (SEM). However, as shown in Fig. 3.4, these detection methods can vary due to the

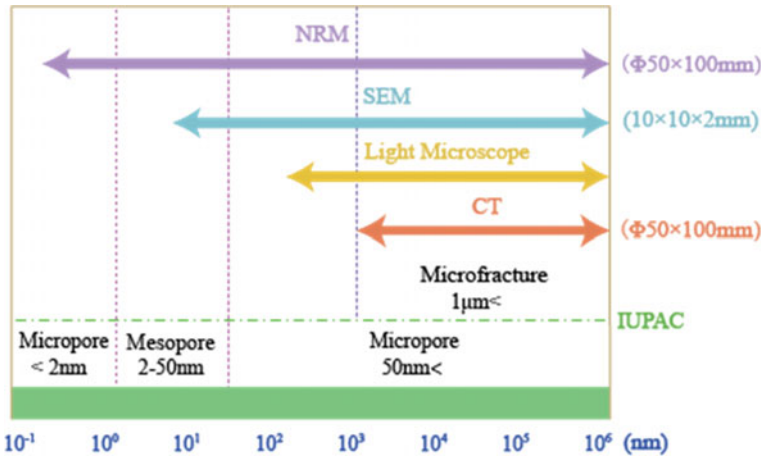


Fig. 3.4 Multiscale pore-fracture characterization techniques

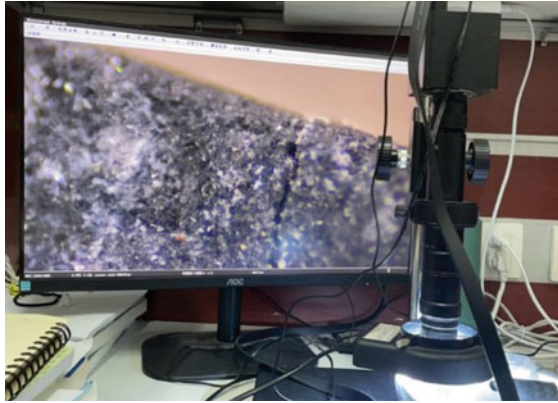
limitation of the sample size or the scanning accuracy. In detail, CT scanning can characterize the internal structural characteristics of rocks, but its accuracy is limited to the micromillimeter scale. Although the microscope and SEM can show the micro and nano rock scale structure, they can only observe the rock surface morphology and require a small sample size. Under high pore pressure stress, shale pores and cracks show strong capillary force, which affects the mechanical properties of rocks and misleads the analysis results. Herein, it is necessary to observe and describe the structural characteristics of shale pores and fissures by comprehensively using microscopy, CT scanning, and SEM at different scales.

(i) Microscopic examination

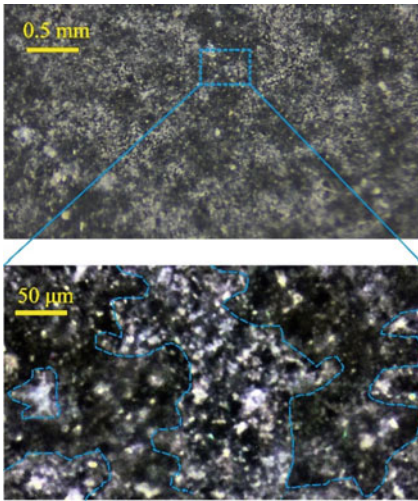
Under natural light (non-polarized light) irradiation, the surface defects and their distribution of shale samples are directly observed with a microscope. As shown in Fig. 3.5a, it can be observed that the two types of shale are mainly composed of a brownish matrix and bright white phenocrysts. Longmaxi shale particles are evenly distributed, without fracture holes, and local bright white sheet-distributed calcite and dolomite debris (Fig. 3.5b). Compared with Longmaxi shale, Lushan shale is mainly composed of a light gray matrix, with locally developed pores whose aperture change range is larger (10–600 μm) (Fig. 3.5c in red dotted line). The locally developed pores are formed by the complex uneven cementation between white muscovite (light green dotted line), yellow-green chlorite (blue dotted line) and shale matrix (brown material), which is conducive to the transmission and adsorption of reservoir resources.

(ii) CT scan imaging

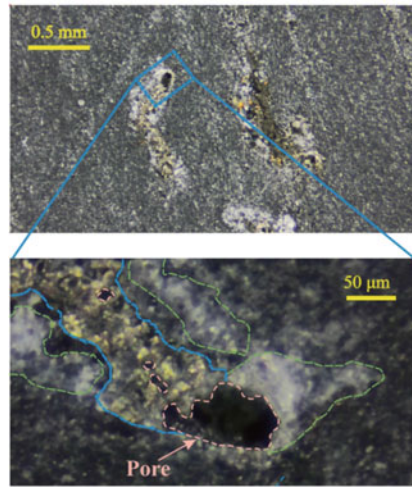
In the CT test, the three-dimension micro focal industry CT analyzer was used to scan the complete cylindrical sample with Φ 50 mm × 100 mm. As shown in Fig. 3.6, the



(a) LED natural light microscopy interface



(b) Longmaxi Shale



(c) Lushan shale

Fig. 3.5 Results of microscopic observation of shale surface under natural light

CT scanner is CD-130BX/CT series, with a spatial resolution of 5–10  $\mu\text{m}$ , and can accommodate a sample with a maximum diameter of 130 mm and a maximum mass of 50 kg. The CT scanner with integrated protective structure design, convenient installation, good safety, and strong environmental adaptability can quickly, high-resolution, and directly 3D scan, which meets the precision requirements of micro millimeter scale structure detection of shale pores and fissures.

As shown in Fig. 3.7, the gray material represents a rock matrix with high density. The Longmaxi shale matrix is gray-white, while the Lushan shale matrix is dark-gray. This difference is related to the radiation intensity of the X-ray source and

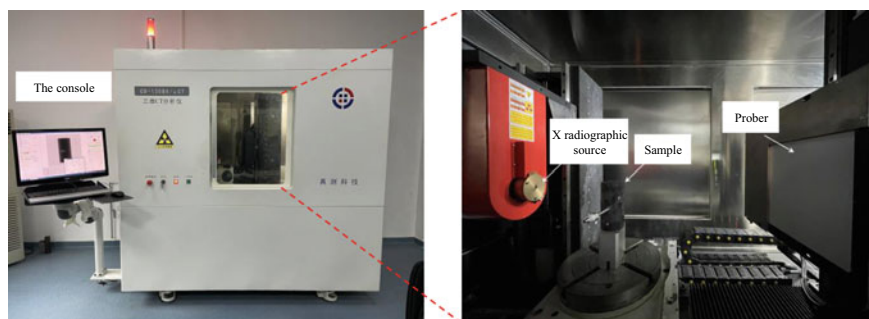


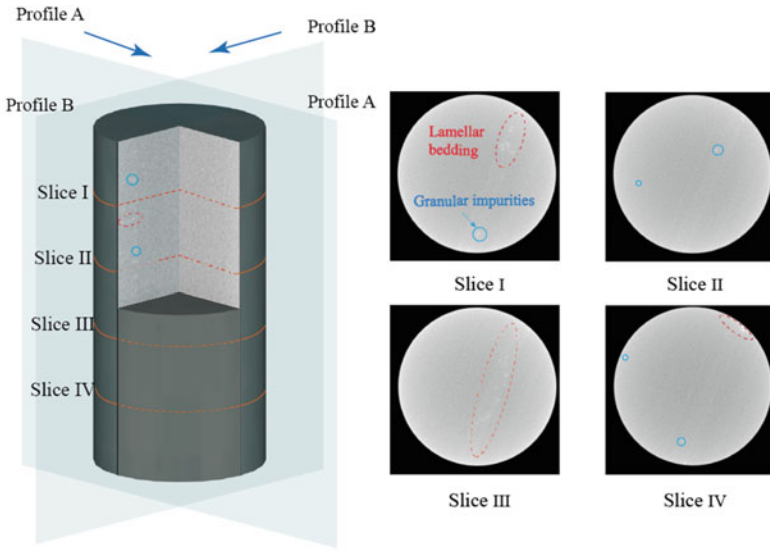
**Fig. 3.6** Microfocus 3D industrial CT detector

does not represent the difference between the actual materials. Both types of shales contain light white spotted impurities (blue circles) and sheet-like distributed bedding (dotted ellipses), which may be caused by the legacy of plant fossils or weak inter-layer accumulation during diagenetic deposition. In contrast, Longmaxi shale has good homogeneity, while Lushan shale, with more granular impurities and schistose beddings, has poor homogeneity. Combined with the XRD analysis results, it is speculated that the main components of this heterogeneity are inadequately cemented illite clay minerals. On the whole, there are no obvious microcracks and holes in the two types of shale, indicating that the two samples are complete and of good quality. However, their internal structures have some differences, indicating the importance of the subsequent comparison of different types of shale on the test results.

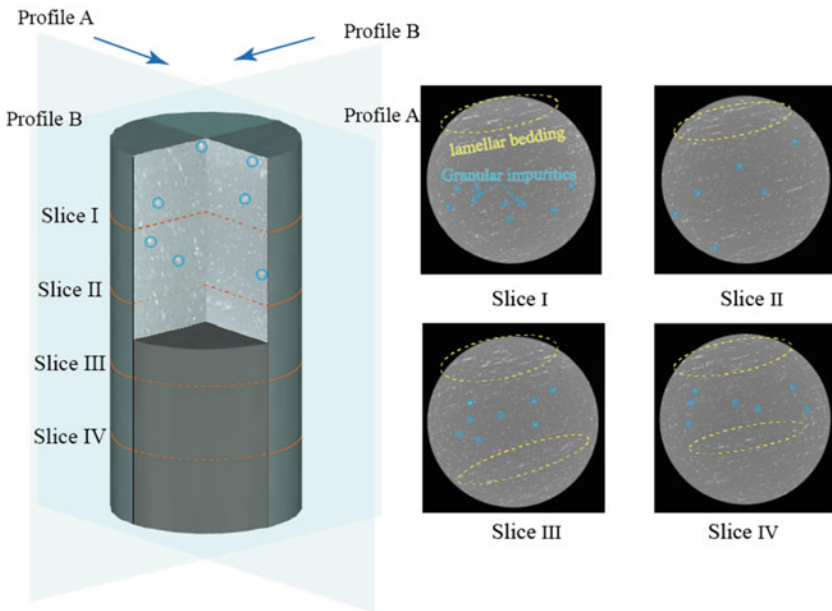
### (iii) SEM observation

As shown in Fig. 3.8, the sheet shale sample was sprayed with gold to eliminate the electronic charging effect on the surface of the material and enhance the electrical conductivity of the rock material. Subsequently, the microstructural morphology of the pores and fissures of the sample was observed under the JEOL JSM-7800F field emission scanning electron microscope in Chongqing University. In general, according to the geological genetic differences, shale pores can be divided into organic matter pores, intergranular pores and intergranular pores [7, 8], and microcracks can be divided into matrix companion cracks, diagenetic shrinkage cracks, tectonic stress cracks (bedding cracks and angle cracks) and other cracks [9]. The EDS energy spectrometer was used to analyze the X-ray characteristics of the mineral elements under the specified scale of the sample, and the pore and microcrack types in the sample can finally be determined according to the XRD analysis results.

Figure 3.9 shows the observation results of shale pore structure under the microscope. It can be seen that the pore morphology of the two types of shale is dominated by intragranular pores (yellow arrow points) and intergranular pores (light blue arrow points). The intragranular pore usually refers to the pore formed inside the particle. The intragranular pores with irregular shapes and pore sizes between 0.5 and 3  $\mu\text{m}$  observed in Longmaxi shale are mainly developed in the calcite. Such intragranular



(a) Longmaxi Shale



(b) Lushan Shale

**Fig. 3.7** Comparison of CT sections of intact specimens between Longmaxi shale and Lushan shale

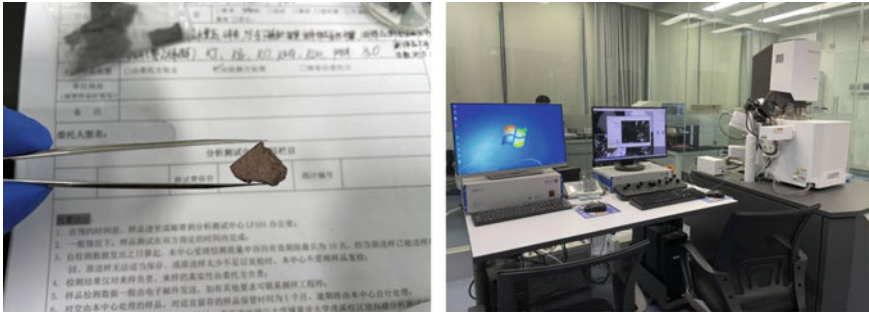


**Fig. 3.8** Photographs of the shale sample after gold spraying and the scanning electron microscope

pores are mostly formed by the dissolution of carbonate or alkane organic acid [10], which vary greatly in depth. In addition to the intragranular pore formed by carbonate dissolution, the intergranular pore developed between thin layered illite and other clay minerals (Fig. 3.9b), with a width between 0.2 and 1  $\mu\text{m}$ , is also observed in Lushan shale. The intergranular pore appears in a slit shape and is mostly formed by a series of tectonic geological effects such as diagenetic evolution and biochemical transformation [11]. Intergranular pores are formed between different mineral particles or between minerals and organic matter. Both types of shale have more interparticle pores, which are mostly found in the contact cementing zone between different mineral particles like quartz, illite, calcite, etc. The pore shape is irregular, mainly depending on the shape of pore particles; the variation range of pore size is large, between 1 and 10  $\mu\text{m}$ , affected by the joint influence of formation into rock transformation and interparticle cementing. Compared with the isolated intergranular pores, the intergranular pores have a larger pore size and better connectivity. When the content of intergranular pores in the selected shale is large, it is conducive to forming an effective pore network and promoting the migration and precipitation of alkanes.

Micro-nano scale crack structure of shale is the key to connecting matrix pores and forming a complex fracture network in reservoir stimulation. As shown in Fig. 3.10, both types of shale develop effective microcracks ranging from nano-scale to micrometers-scale, which are specifically manifested as bedding cracks, transgranular cracks and intergranular cracks. The bedding crack develops at a scale of several hundred micrometers (Fig. 3.10a, c), and its contour is basically the same as the lamellar edge. Such microcracks are usually formed by the accumulation of sheet clay mineral matrix in the process of sedimentation. Clastic minerals or organic matter with weak cohesive force filled between lamellas are easy to flake off along mineral bedding under external force [12]. In Fig. 3.10b, d, grain inner cracks and grain margin cracks are distributed at tens of micron scales of shale samples, extending along the particle profile and penetrating matrix, respectively [13]. This kind of crack is usually long, narrow, and tortuous, with no filling minerals, and its opening varies with the propagation path at the range of 2–9  $\mu\text{m}$ , and its length is mostly less than 50  $\mu\text{m}$ .

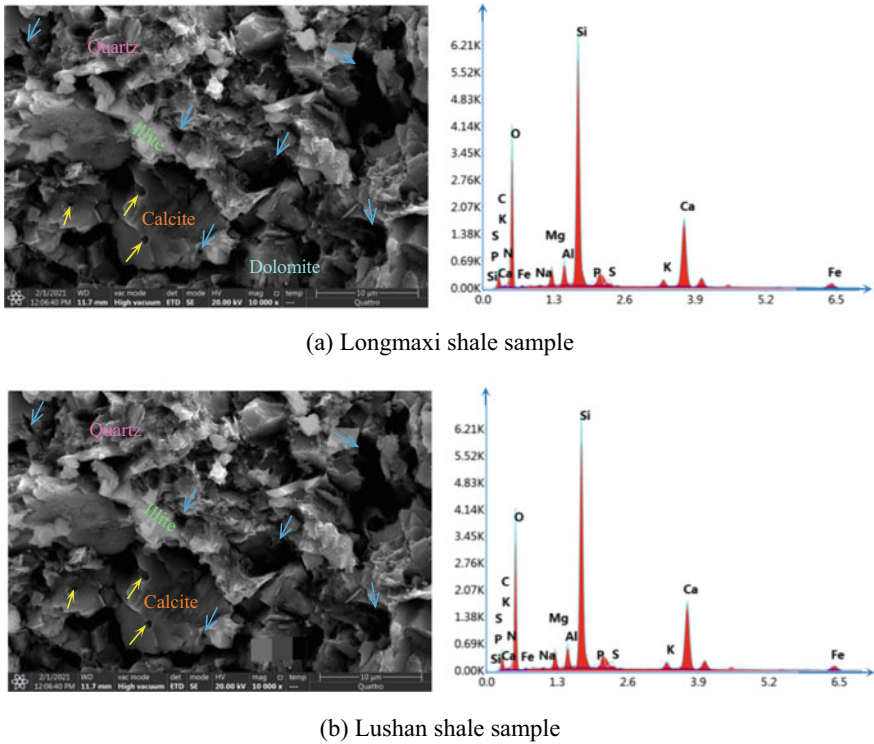


**Fig. 3.9** Shale pore types, mineral distribution and X-ray energy spectrum

In addition, grain inner cracks and grain margin cracks do not always occur independently. For example, in Fig. 3.10d, microcracks are respectively grain margin crack, grain inner crack, and grain margin crack from top to bottom. The opening of grain margin crack is the largest, which is related to the uneven external forces caused by thermal expansion, dehydration shrinkage, or tectonic evolution of shale matrix during the formation of microcracks. On the whole, the microcracks of two types of shale are developed, but the size and length of the local microcracks are limited, and the macro crack structures are not formed in a large range. This type of crack structure of reservoir is conducive to effectively communicating the organic matter pores in the matrix in reservoir stimulation, forming migration channels of shale gas, which accelerates the precipitation and migration of alkane resources and improves the shale gas extraction rate.

Through the above comparison, it can be found that the environmental conditions of reservoirs directly affect the mineral composition of rock and the structural morphology of the matrix. Therefore, even if the same construction parameters are selected in the fracturing process, the hydraulic fracturing results of shale will still be significantly different. The different hydraulic fracturing effectiveness resulting

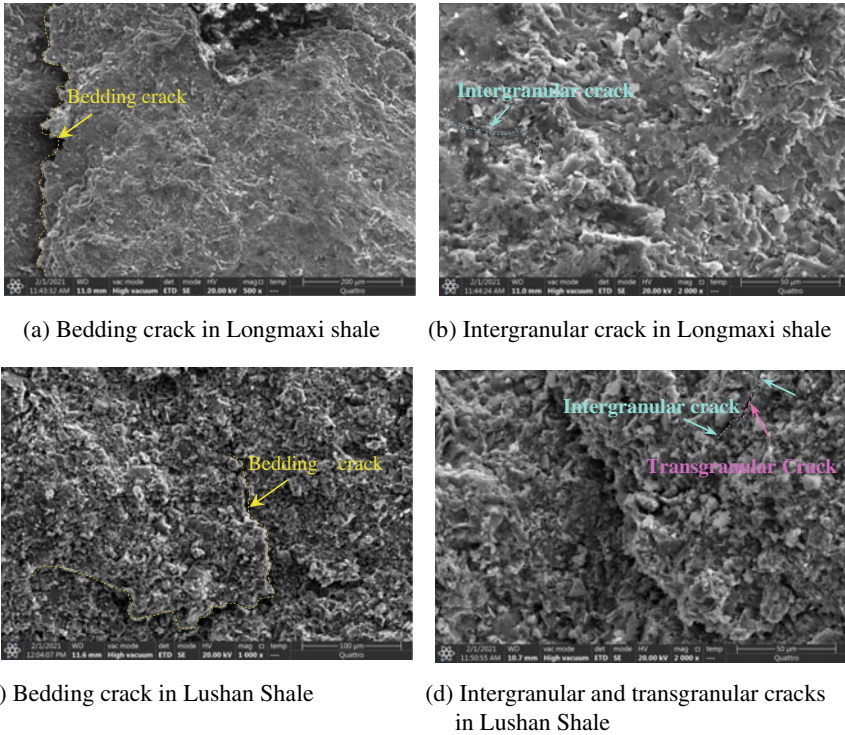


**Fig. 3.10** Characteristic of the microcracks in shale samples

from differences in the reservoir environment are discussed in detail in Sect. 3.4.3 of this chapter.

### 3.3 Determination of the Physical and Mechanical Parameters of Shale

The basic physical parameters of Lushan shale as the comparative group have been discussed in detail by Shang et al. [14]. Therefore, the basic physical properties of Longmaxi shale as the research object are tested and analyzed as follows. Strictly speaking, the physical and mechanical parameters of the rocks should reflect the high temperature and high-pressure characteristics of the in-situ reservoir, so as to have a reference value for the actual construction of the project. However, considering the difficulty of in-situ sampling and test instruments, we focus on fracture propagation form and ignore the influence of high temperature and high pressure, therefore the following physical and mechanical parameters of shale (such as porosity, permeability, uniaxial compressive strength, cohesion, internal friction angle, etc.) are based

on laboratory conditions under the room temperature and pressure. Although the indoor conditions are quite different from the actual shale occurrence environment, the test results can still provide a reference for the subsequent design of the indoor hydraulic fracturing scheme [14–16].

### 3.3.1 Porosity

Porosity is an important indicator to measure the degree of rock pore structure development, which affects the storage and adsorption of shale gas and the strength and permeability of shale. Therefore, the porosity and permeability of the shale specimen should be clarified before hydraulic fracturing. To ensure the reliability of the measurement results, the porosity was measured by the gaseous method and the saturated mass method, respectively.

Nitrogen gas is selected as the measuring medium. The used shale sample is cylindrical with 50 mm in diameter and 100 mm in height. Before the test, the sample was placed in a 105 °C constant temperature drying incubator for 24 h, and then the shale porosity test was conducted on the BRS-II pulse tester. The BRS-II type pulse tester can automatically measure the porosity of shale specimens in the Hassler Holder based on the Boyle law. Figure 3.11 shows a schematic diagram of the porosity measurement. A total of five sets of porosity tests were conducted, and the porosity results are summarized in Table 3.2. From Table 3.2, the average pore volume is 4.73 mL, and the average porosity is 2.39% with a standard deviation of 0.843%, indicating that the test results are less discrete.

The saturated mass method is to calculate the pore volume in the shale specimen by using the definition of density. The calculation formula is

$$n = \frac{m_w - m_s}{\rho V_s} \quad (3.1)$$

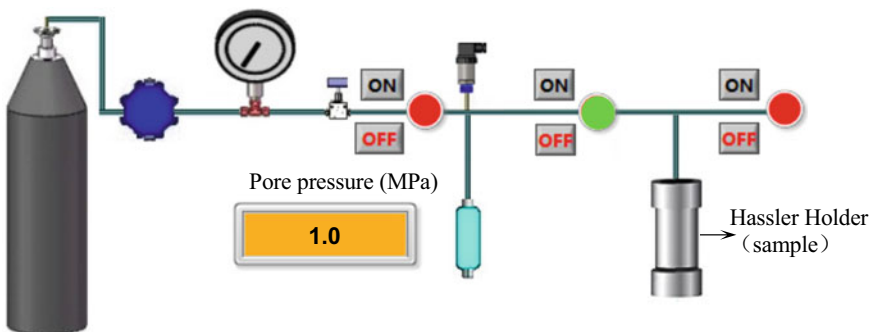


**Fig. 3.11** Schematic diagram of the porosity measurement of shale cores

**Table 3.2** Results of porosity measurement by gaseous method

No.	$H/mm$	$D/mm$	Pore volume/mL	Prosity/%
PG-1	100.12	50.05	4.6	2.33
PG-2	100.22	50.01	4.1	2.08
PG-3	100.26	50.02	5.4	2.74
PG-4	100.13	50.12	7.3	3.69
PG-5	100.19	50.20	2.2	1.11
Average	100.184	50.08	4.72	2.39
Standard deviation	0.053	0.071	1.66	0.843

**Table 3.3** Results of porosity measurement by mass fraction method

NO	$H/mm$	$D/mm$	Dry sample mass $m_s/g$	Mass after saturation $m_w/g$	Porosity/%
PM-1	100.04	50.08	514.752	520.547	2.898
PM-2	100.11	50.16	519.518	525.420	2.977
PM-3	100.01	50.11	517.364	522.955	2.835
Average	100.053	50.117	517.211	522.974	2.903
Standard deviation	0.042	0.033	1.949	1.989	0.058

where,  $m_w$  is the mass of the saturated specimen,  $m_s$  is the mass of the specimen treated at 105°C for 24 h before saturation,  $\rho$  is the density of water at normal temperature and pressure, which takes 1 g/cm<sup>3</sup>, and  $V_s$  is the sample volume. After calculation, the average porosity of the rock is 2.903%, which is similar to the gas measurement result (2.39%), so the selected shale is a dense rock with low porosity (Table 3.3).

To further analyze the pore size of Longmaxi shale, the NMR technology was used to measure the relative distribution of Longmaxi shale pores. Based on the relationship between the transverse relaxation time of hydrogen nuclei (<sup>1</sup>H) of the fluid inside the rock pores and the pore radius, the pore size distribution of different pores can be indirectly obtained by using NMR, realizing the analysis of rock microstructure [14]. NMR techniques can characterize pores at a sub-micron scale and offer unique advantages in analyzing small, complex pore structures [15, 16]. Before the test, the samples were placed in a saturator under a vacuum for 24 h to saturate them with water. and then the MRI test was carried out in the MacroMR12-150H-I nuclear magnet core analysis instrument (Fig. 3.12) produced by Suzhou Numai Technology Company. The magnetic field strength was 0.3 T, with the dominant frequency of 12 MHz, and an RF delay time of 0.02 ms.

The wave peak number, distribution form, continuity, and trend of the T<sub>2</sub> spectrum reflect the development characteristics of pores at all levels in the sample. Figure 3.13 shows the signal intensity of the nuclear magnetic T<sub>2</sub> spectrum with of shale specimens changing with transverse relaxation time. The T<sub>2</sub> spectrum of two specimens

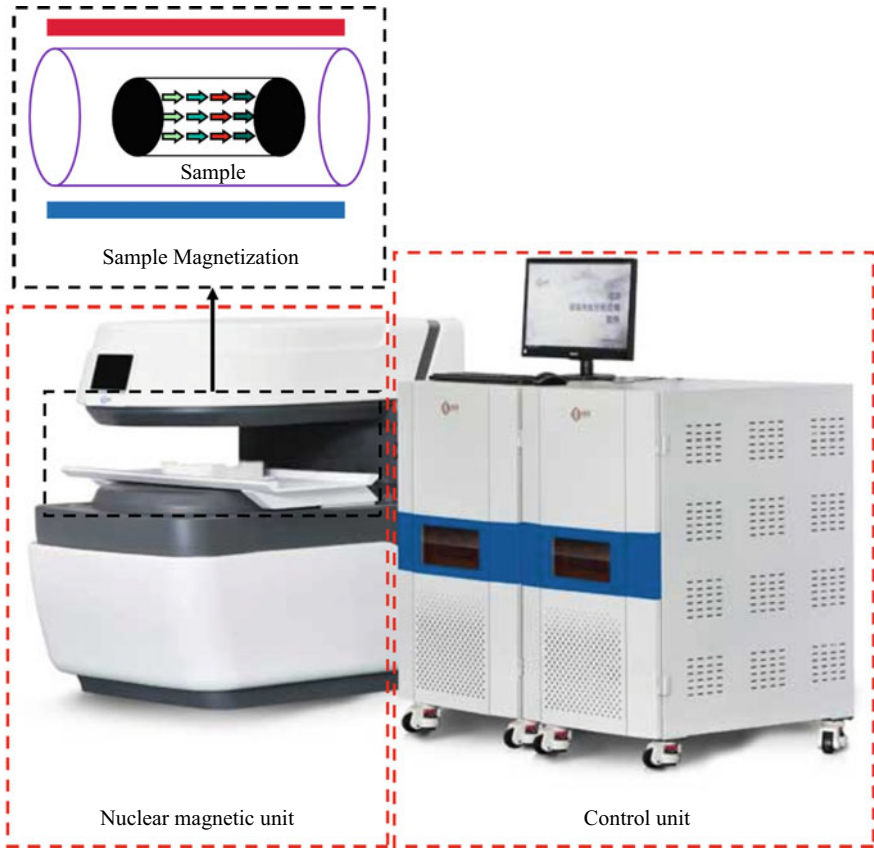


Fig. 3.12 Schematic diagram of nuclear magnetic resonance system

is mainly in the asymmetric discontinuous bimodal form. The signal intensity of the right peak is far less than that of the left peak. The relaxation time range of the left peak is 0.1–10 ms, the relaxation time range of the right peak is 10–100 ms, and the spectral peak area of the left peak accounts for nearly 98.7% of the total area. From the trend of the  $T_2$  spectrum curve, there should be mainly two types of pores divided by the range of pore size in the sample, and the connectivity of the two pores is poor.

Based on the signal intensity parameters of the  $T_2$  spectrum, the ratio relationship between the pore radius and the signal intensity is used to convert the  $T_2$  spectrum curve into the pore throat distribution curve to further analyze the scale size of the pore structure. Its conversion relationship is as follows:

$$r = CT_2 \tag{3.2}$$

where,  $C$  is the conversion coefficient,  $r$  is the pore radius, and  $T_2$  is relation time.

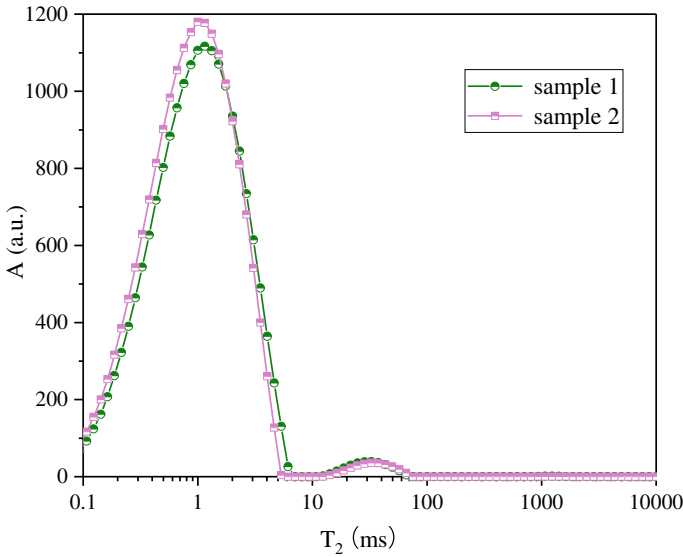


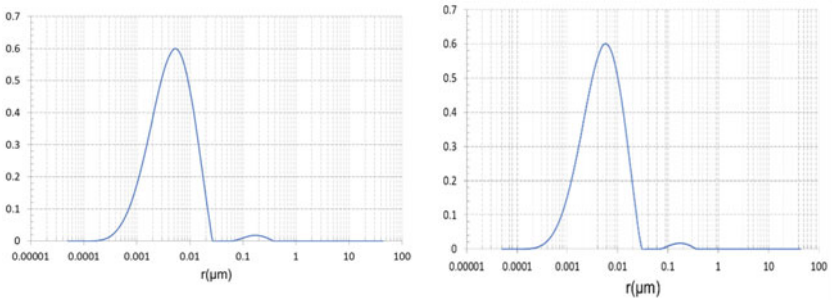
**Fig. 3.13** Nuclear magnetic resonance  $T_2$  spectrum of shale specimens

As shown in Fig. 3.14a, b, comparing the pore throat radius distribution of two samples, it can be seen that the pore throat of shale specimens is concentrated at the radius of 0.001–0.01  $\mu\text{m}$ . Based on the definition of IUPAC on micropores (< 2 nm), medium pores (2–50 nm), and macro pores (> 50 nm), the pore radius distribution of two shale specimens can be counted to obtain the percentage of different types of pores in the total pore volume. As shown in Fig. 3.14c, the pores in the sample are dominated by medium pores, followed by micropores, with the minimum proportion of macropores. Combined with the  $T_2$  spectrum curve characteristics, it is continuous in the range of micropores and medium pores, indicating that the connectivity between micro and medium pores is good, while the macropore distribution is relatively independent, demonstrating that macropores have poor connectivity with other types of pores.

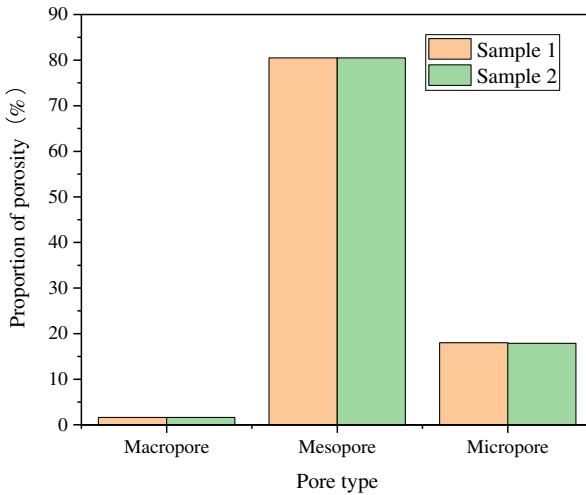
### 3.3.2 Permeability

Permeability, an important indicator to measure the permeability of the rock and evaluate the conductivity of reservoir rocks, is an indirect reflection of the distribution state of rock pore structure, which has been widely used in deep energy exploitation, infrastructure engineering and nuclear waste storage and other fields.

The transient pressure pulse method (referred to as the transient method) is a common method to determine the low permeability rock (<  $10^{-19}$   $\text{m}^2$  [17]), whose testing principle is shown in Fig. 3.15. The rock specimen dried in a 105  $^\circ\text{C}$  for



(a) Pore throat radius distribution of sample 1 (b) Pore throat radius distribution of sample 2



(c) Proportion of different porosity

**Fig. 3.14** Pore throat radius distribution and relative content of different pore types of shale specimens

24 h is put into a holder, and a certain amount of initial fluid pressure is injected at both ends of the specimen to balance the upstream and downstream pressure. After the upstream and downstream pressures are stabilized, the constant pulse pressure is applied to the upstream end of the sample. The permeability of the rock is calculated by recording the upstream and downstream pressure changes of the sample using the following equation [18].

$$K = \frac{\alpha \mu \beta L}{\left(\frac{1}{v_u} + \frac{1}{v_d}\right) A} \tag{3.3}$$

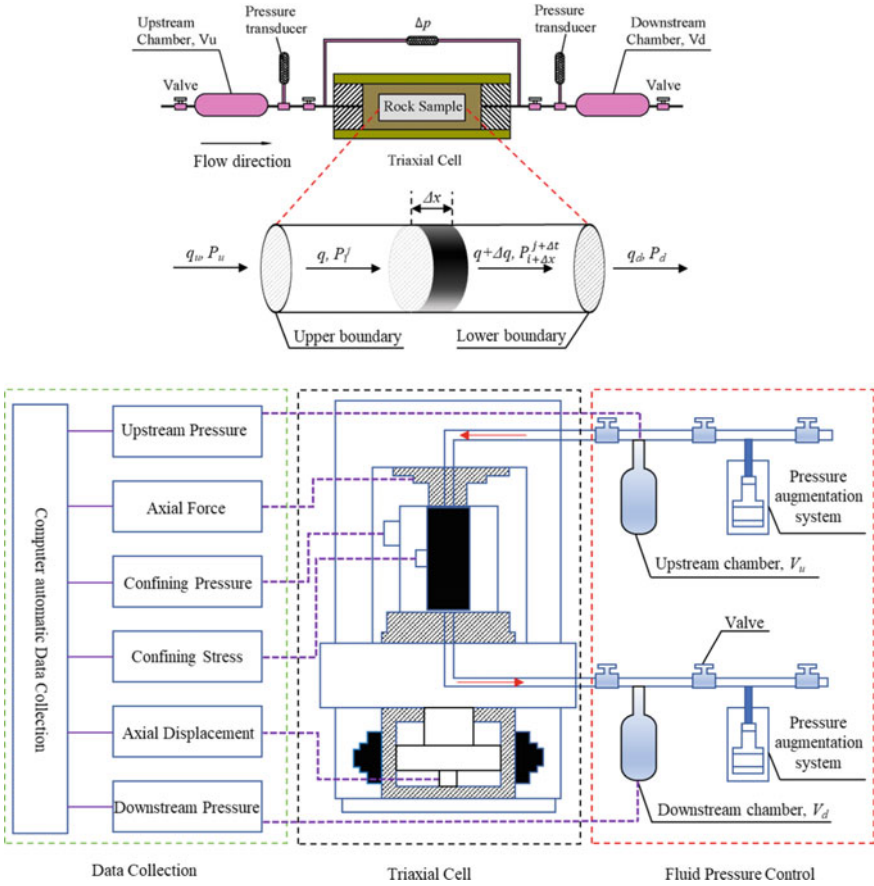


Fig. 3.15 Schematic diagram of the permeability measurement of shale cores

where,  $K$  is the rock permeability (permeability coefficient),  $\mu$  is the gas dynamic viscosity,  $\beta$  is the fluid compression coefficient,  $L$  is the sample length,  $V_u$  and  $V_d$  are the upstream and downstream gas chamber volumes, whose value is  $2.199 \times 10^{-5} \text{ m}^{-3}$  and  $2.102 \times 10^{-5} \text{ m}^{-3}$ , respectively,  $A$  is the sample's cross-sectional area,  $\alpha$  is the attenuation coefficient, which can be calculated by upstream and downstream pressure difference [19], and its calculation formula is expressed as

$$\alpha = -\frac{1}{t} \ln \frac{P_u(t) - P_d(t)}{P_u(0) - P_d(0)} = -\frac{1}{t} \ln \frac{\Delta P(t)}{\Delta P(0)} \quad (3.4)$$

where  $t$  is the fluid permeability time,  $P_u(t)$  and  $P_d(t)$  correspond to the upstream and downstream pressure values at time  $t$  ( $t = 0$  corresponds to the initial time), and the upstream and downstream pressure differences at different times are  $\Delta P(t)$  and  $\Delta P(0)$ , respectively.

**Table 3.4** Results of permeability measurement by pulse-test method

$H/\text{mm}$	$D/\text{mm}$	$\Delta P(0)/\text{MPa}$	$\Delta P(t)/\text{MPa}$	$t/\text{s}$	$\mu/\mu\text{Pa}\cdot\text{s}$	$\beta/10^{-4} \text{MPa}$	$K/10^{-22} \text{m}^2$
99.91	50.07	0.27	0.08	44,794	17.975	4.642	1.172
100.07	50.10	0.33	0.12	61,524	17.996	4.398	2.556
100.03	50.03	0.58	0.28	21,380	18.136	4.329	1.551
Average permeability							1.76
Standard deviation of permeability							0.583

Table 3.4 makes statistics on the upstream and downstream pressure decay trend, the gas permeability time, the dynamic viscosity of the gas, and the compression coefficient. According to Eqs. (3.3) and (3.4), the average permeability of the shale specimens is  $1.76 \times 10^{-22} \text{m}^2$  with a standard deviation of  $0.583 \times 10^{-22} \text{m}^2$ .

To sum up, the rocks of the Longmaxi shale gas reservoirs in the Changning area are dense in structure, characterized by an ultra-low porosity whose average value is 2.903% and an ultra-low permeability whose average value of  $1.76 \times 10^{-22} \text{m}^2$ .

### 3.3.3 Basic Mechanical Properties of Longmaxi Shale

The basic mechanical properties of the rock, such as uniaxial compressive strength, elastic modulus, Poisson ratio, splitting tensile strength, cohesion and internal friction angle, are the macroscopic characterization of the bonding effect of microscopic mineral and the stress evolution of the pore throat structure. Mastering the basic mechanical properties of the reservoir rocks is the basis for the subsequent analysis of the hydrofracturing mechanism and the dynamic process of the initiation, propagation, and intersection of hydraulic fracture, which can provide an important reference for the subsequent theoretical calculation of the hydrofracturing and the calibration of simulation parameters of rock fracture evolution.

The basic mechanical properties of shale were tested on the DSZ-1000 rock mechanics test machine as shown in Fig. 3.16. The DSZ-1000 type rock mechanics test machine is composed of hydraulic power system, servo control system, data monitoring and acquisition system, test platform and operating platform, which can perform mechanical tests such as uniaxial compression, triaxial compression, rock rheology, cyclic loading and unloading, etc. The maximum axial pressure is 1000 kN, whose adjustable loading rate range is 0.1–100 mm/min, the maximum circumferential confining pressure is 60 MPa, whose loading rate range is 0.1–60 MPa/min, and the measurement accuracy range of pressure and displacement is  $\leq \pm 0.5\% \text{FS}$ . The rigidity of the testing machine is 5 GN/m. The LVDT circumferential and axial strain gauges with an accuracy of 0.25% FS are installed, and they can withstand up to 60 MPa hydrostatic pressure, meeting the technical requirements for testing the basic mechanical parameters of rocks.

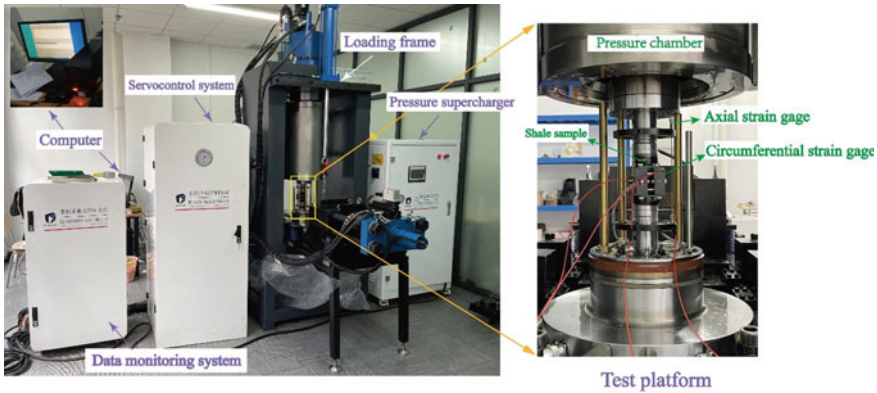


**Fig. 3.16** DSZ-1000 rock mechanics test system

(i) Uniaxial compressive strength, elastic modulus, and Poisson ratio

With reference to the methods recommended by the International Society for Rock Mechanics (ISRM), cylindrical samples with a diameter of 50 mm and a height of 100 mm are selected for uniaxial compressive strength, elastic modulus and Poisson ratio tests of shale. To reduce the discrete error of sampling, three sets of uniaxial compression tests were performed successively, and the sample numbers were UC-1, UC-2 and UC-3. Displacement mode with a loading rate of 0.1 mm/min was used to control the loading process. The sample is sheathed with a heat-shrinkable tube to prevent the splashing of fragments when the rock sample is damaged, causing accidental injury to the tester and damaging the instruments and equipment.

Figure 3.17 shows the stress–strain curve of uniaxial compression. Compared with the uniaxial compression stress–strain curve of conventional rock (such as sandstone) [20], the curvature of initial axial strain of Longmaxi shale is low, and its circumferential strain increases slowly. The overall change of curve in the compaction process is not obvious, indicating that the deformation caused by pore compaction is small, the shale matrix is dense, and the structure of pore microcracks in the sample is not developed. In terms of the rock deformation response, the deformation in the linear elastic stage of the rock accounts for a large proportion. With the increase of axial strain, the growth rate of circumferential strain increases, and the number of microcracks in the rock increases. Subsequently, the rock was almost fractured directly beyond the yield stage, accompanied by a significant splitting sound, and no residual strength appeared after the peak, showing obvious brittle characteristics. In terms of the fracture morphology of intact shale (Fig. 3.18), the tensile failure is dominant in three samples, and -3 specimens UC-2 and UC have a single inclined plane shear failure. The shear plane is generally short, which may be related to the orientation of potential bedding in the specimen. The vein-like secondary fractures are attached around the main fracture. The obvious compression fragmentation and flake exfoliation can be seen after removing the heat shrinkage tube (Fig. 3.18d). The thickness of the fragments is less than 10 mm, and the fragments whose length is less

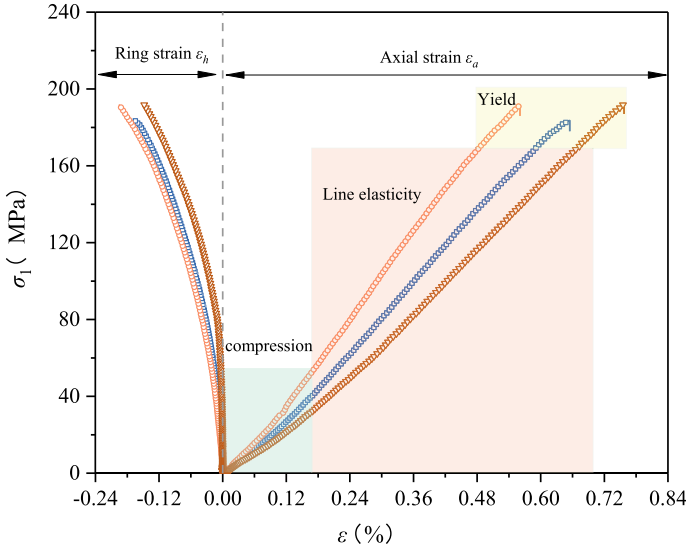


**Fig. 3.17** Curves of stress versus strain during the process of uniaxial compression

than 60 mm account for 94% of the total, indicating that the degree of compression crushing is relatively high.

The geometry dimensions and the measured mechanical parameters of the uniaxial compression of the specimen are summarized in Table 3.5.  $\rho$  is the density of the specimen,  $\sigma_p$  is the uniaxial compressive strength of the rock,  $E$  is the elastic modulus of the rock,  $E_{50}$  is the secant slope of the stress–strain curve at 50% axial stress,  $\nu$  is the Poisson ratio,  $\varepsilon_{a-max}$  is the peak of axial strain,  $\varepsilon_{h-max}$  is the peak of circumferential strain. From the standard deviation calculated from the three sets of test data, the shape and density of the selected specimens are consistent. The standard deviation of the measured mechanical parameters is within a reasonable range, indicating that the shale specimens have a uniform texture and stable properties, which can be used for the subsequent study on the change of external factors in the shale hydraulic fracturing process. As can be seen from Table 3.5, the average uniaxial compressive strength of shale samples is 189.25 MPa, the average elastic modulus is 31.29 GPa, and the average Poisson ratio is 0.119.

(ii) Splitting tensile strength

The Brazilian splitting method is commonly used to indirectly measure the tensile strength through the lateral tension of rock caused by vertical compression. The shale disc sample with a diameter of 50 mm and a thickness of 25 mm can be subjected to the Brazilian splitting test on the DSZ-1000 rock mechanics testing machine by using the fixture shown in Fig. 3.19a. The fixture is made of solid steel, with strong rigidity, small deformation, and low storage elastic energy. It is embedded groove and equipped with a filler strip with a diameter of 1 mm to ensure that the specimen

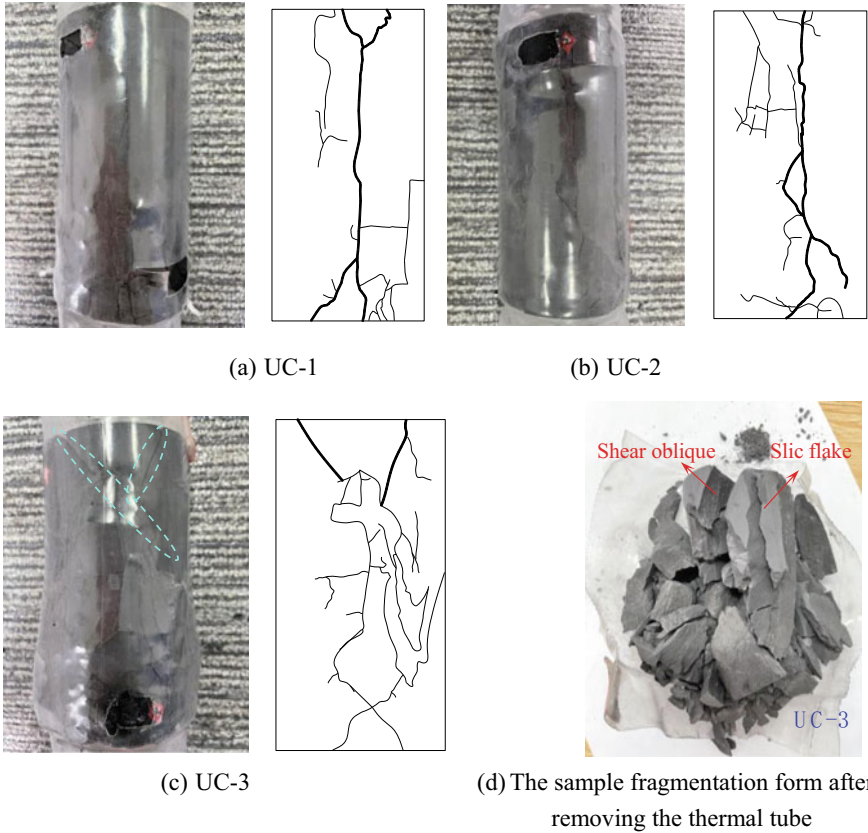


**Fig. 3.18** Fracture morphology of shale samples under uniaxial compression state

cracks along the centerline. During the test, the initial pressure of 100 N is loaded to fix the specimen. Then, the specimen is loaded at a rate of 0.05 mm/min in a displacement-controlled manner until the specimen is broken.

The specimen bears the line load in the thickness direction, and the tensile strength calculation formula is

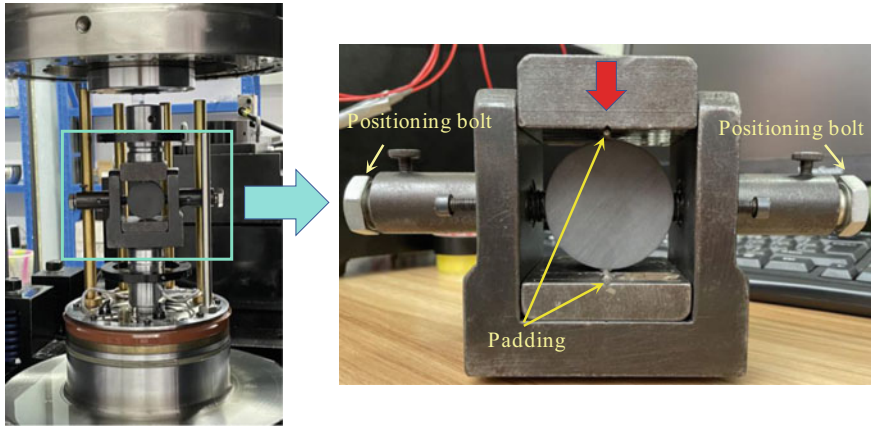
$$\sigma_t = \frac{2P}{\pi DT} \tag{3.5}$$

where  $P$  is the maximum axial load,  $D$  is the specimen diameter, and  $T$  is the specimen thickness.

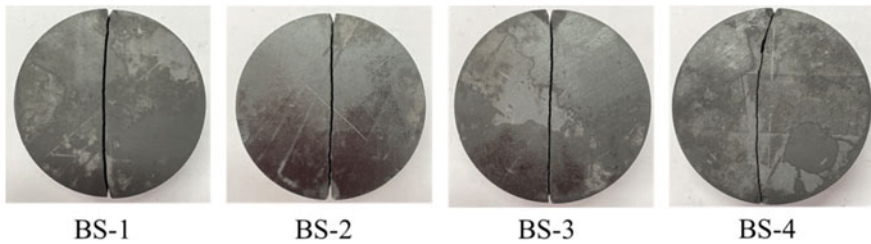
The splitting failure effect of the disc specimen is shown in Fig. 3.19b. It can be found that the four groups of specimens are basically subject to symmetrical tensile failure along the loading direction, and the specimen is divided by the fracture along the loading direction, forming a relatively regular linear fracture. Except for a small amount of flaking fragments at the loading point, no fragments and rock debris

**Table 3.5** Summary of shale mechanical parameters from uniaxial compression tests

No.	$H/mm$	$\Phi/mm$	$\rho/g\cdot cm^{-3}$	$\sigma_p/MPa$	$E/GPa$	$E_{50}/GPa$	$\nu$	$\varepsilon_{e-max} (10^{-3})$	$\varepsilon_{h-max} (10^{-3})$
UC-1	100.31	50.15	2.642	183.76	30.61	27.35	0.120	6.54	1.69
UC-2	100.26	50.24	2.634	191.54	34.93	34.15	0.185	5.61	1.96
UC-3	100.33	50.08	2.631	192.46	28.34	23.46	0.052	7.57	1.49
Average	100.3	50.16	2.636	189.25	31.29	28.32	0.119	6.57	1.71
Standard deviation	0.029	0.065	0.005	3.902	2.733	4.418	0.054	0.801	0.193



(a) Brazilian splitting test device



(b) Broken form

**Fig. 3.19** Brazilian splitting test of shale disks

occurred elsewhere, indicating that the damage to the specimen is a typical tensile failure. Using Eq. (3.5) and Table 3.6, the average split tensile strength of shale samples is 6.71 MPa and its standard deviation is 1.147.

**Table 3.6** Results of Brazil splitting tests

No.	Diameter $\Phi$ /mm	Thickness $T$ /mm	Peak load $P$ /kN	Splitting tensile strength $\sigma_t$ /MPa
BS-1	50.12	24.99	13.40	6.81
BS-2	50.04	24.97	13.18	6.72
BS-3	50.08	25.03	9.91	5.03
BS-4	50.22	24.96	16.28	8.27
Average	50.12	24.99	13.19	6.71
Standard deviation	0.067	0.027	2.256	1.147

## (iii) Cohesion and internal friction angle

Based on the triaxial compression loading module of the rock mechanical test system shown in Fig. 3.16, the conventional triaxial compression test of shale is carried out to obtain the cohesion and internal friction angle of shale. Three sets of shale cylinder specimens ( $\Phi 50 \times 100$  mm) marked TC-1, TC-2, and TC-3, respectively, were taken, corresponding to the confining pressure ( $\sigma_{3c}$ ) of 5, 10, and 20 MPa [20]. The confining pressures of different gradients were set to calculate cohesion and internal friction angle using the Mohr strength envelope theorem. The stress control mode with a loading rate of 1 MPa/min was used to control the confining pressure. It remained constant when the confining pressure increased to the target value. Then, the displacement control mode with a loading rate of 0.1 mm/min was used to increase the axial pressure until the specimen was damaged. The strength and deformation parameters of the rock were recorded in the loading process, and the fracture morphology of the rock was observed.

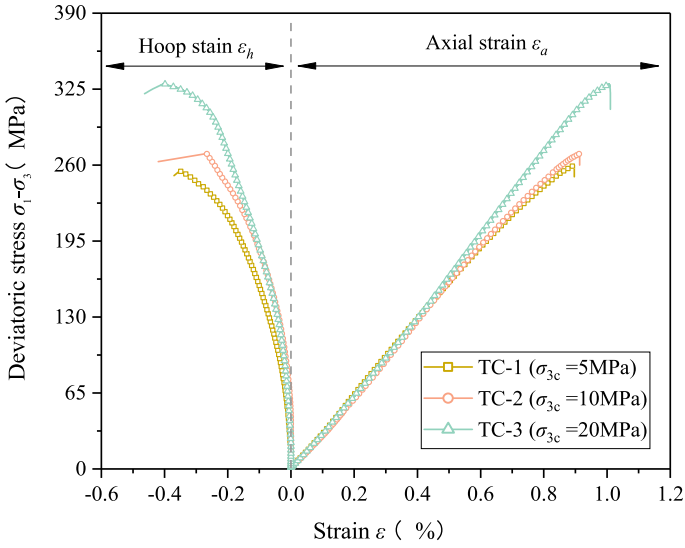
Figure 3.20a shows the stress–strain curve of shale specimens under different triaxial stress states. Compared with the uniaxial compression curve, the curve shown in Fig. 3.20a almost has no the compression stage and directly reaches the linear elasticity stage, which shows that the different stress and strain test curves in the initial compression stage coincide because the pores in the sample have been compacted by the confining pressure before the application of deviatoric stress. With the increase of the confining pressure, the rock elastic modulus increases, and the peak of axial stress also correspondingly increases. The rock volume strain is positive and increases with the confining pressure, indicating that the increase of confining pressure has a positive effect on the increase of rock deformation. Figure 3.20b shows the fracture morphology of the shale specimen after the test. Under the action of confining pressure, only a single oblique main fracture with a small number of secondary fractures was observed in the specimen. After removing the heat shrinkage pipe, the specimens can still maintain strong integrity which differs from the almost complete fracture morphology under uniaxial compression.

The cohesion and internal friction angle are calculated by the Mohr strength envelope theorem [21] based on the statistics of the peak value of axial pressure of each group of samples and the results of the uniaxial compression test (mean value). The calculation equations are as follows:

$$c = \frac{B}{2\sqrt{K}} \quad (3.6)$$

$$\varphi = \tan^{-1} \frac{K - 1}{2\sqrt{K}} \quad (3.7)$$

where  $c$  is the cohesion and  $\varphi$  is the internal friction angle,  $K$  is the slope of the linear fitting curve of the measured data points in the coordinate space between the peak value of axial stress  $\sigma_{1p}$  (longitudinal axis) and the confining pressure  $\sigma_{3c}$  (transverse axis), and  $B$  is the intercept of the fitting curve on the longitudinal axis



(a) Stress- strain curves



TC-1

TC-2

TC-3

(b) fracture morphology

**Fig. 3.20** Curves of stress versus strain and fracture morphology of shale specimens under different confining pressures

which actually represents the uniaxial compressive strength value estimated by the triaxial compression test parameters.

Figure 3.21 shows the linear fitting results of the peak value of the axial stress under different confining pressure conditions. By calculation,  $K$  is 7.259,  $B$  is 208.603, and the fitting accuracy is 0.949, indicating a strong linear correlation between the

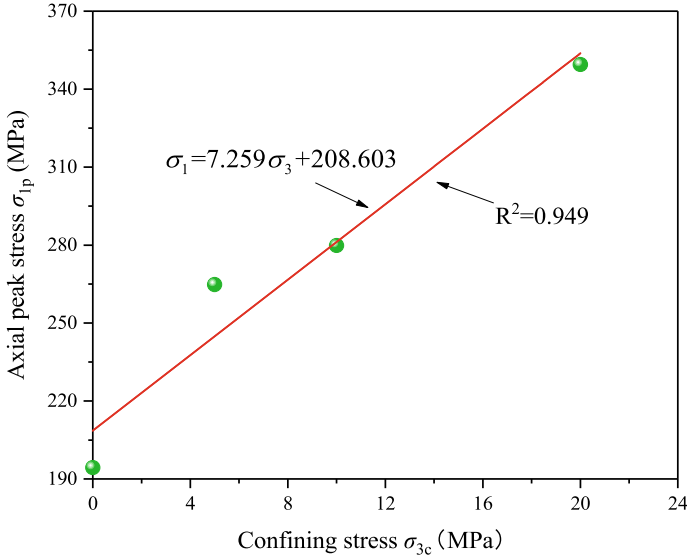


**Fig. 3.21** Peak values of axial stress under different confining pressures

confining pressure and the peak of axial stress. Substituting  $K$  and  $B$  into Eqs. (3.6) and (3.7), the cohesion is 38.71 MPa and the internal friction angle is 49.27. The geometric dimensions, strength, and deformation parameters of shale specimens are summarized in Table 3.7.

### 3.4 Uniaxial Hydraulic Fracturing Characteristics

Under the uniaxial stress conditions, due to the relevant variables being better controlled, the evolution mechanism of initiation and propagation of hydraulic fracture was mainly studied to clarify the formation process and micromorphology characteristics of fracture under different conditions [22]. Before the simulation of the true hydraulic fracturing process in the laboratory, hydraulic fracturing tests under simple and ideal stress conditions are often carried out to eliminate the disturbance effect of different stress states on hydraulic fracturing characteristics [23–26], which directly reflects the mechanical response characteristics of the specimen under external hydraulic injection [23]. Therefore, in this section, the shale hydraulic fracturing tests under the ideal uniaxial stress state were carried out to explore the hydraulic fracture characteristics and fracture propagation law without the confining pressure.

To facilitate fluid injection, a central hole with a 6 mm diameter and 55 mm depth was drilled on one end face of the shale specimen to model the injection hole, as shown in Fig. 3.22. In this injection mode, as the fluid accumulates in the hole, the

**Table 3.7** Size and parameters of strength and deformation of shale specimens used for conventional triaxial compression experiments

No.	$\Phi$ /mm	$H$ /mm	Density/g/cm <sup>3</sup>	$\sigma_{3c}$ /MPa	$\sigma_{1p}$ /MPa	$E_1$ /GPa	$\varepsilon_{\theta\theta\text{-max}}$ (10 <sup>-3</sup> )	$\varepsilon_{\theta\theta\text{-max}}$ (10 <sup>-3</sup> )	$\varepsilon_{v\text{-max}}$ (10 <sup>-3</sup> )	
TC-1	50.14	100.11	2.644	5	264.79	31.14	8.96	3.53	1.9	
TC-2	50.13	100.07	2.642	10	279.83	32.96	9.14	2.67	3.8	
TC-3	50.07	99.98	2.664	20	349.49	35.57	12.07	4.04	3.99	
Cohesive $c$ /MPa										
Internal friction angle $\varphi$ /°										
						38.71				
						49.27				

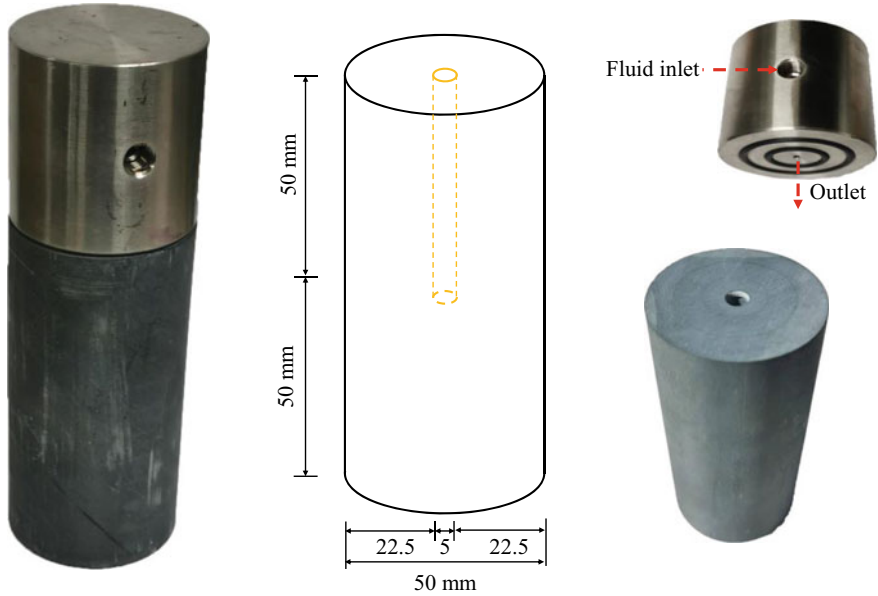


Fig. 3.22 Conventional fracturing method by injecting water from one specimen end face

stress concentration is prone to generate near the fluid outlet, prompting the fracture to initiate at the bottom of the specimen (near the water outlet), rather than the bottom of the drilling hole. Then, as the fluid flows out along the fracture, the subsequent propagation of the fracture cannot be maintained, resulting in incomplete fracturing of the specimen, as shown in Fig. 3.23. In addition, in this injection mode, the entire inner wall of the borehole is in direct contact with the fluid. Under the action of internal high pressure, fluid can penetrate into the rock matrix, which will disturb the subsequent breakdown pressure and fracture morphology of the shale specimen, leading to the experimental results do not truly reflect the hydraulic fracturing performance of the sample. Based on this, the author independently designed the inlet tube seal pipe valve to carry out the uniaxial hydraulic fracturing test by lateral injection. This lateral injection mode can truly reflect the actual (through the bore) hydraulic fracturing process, easy to observe the sample surface fracture propagation morphology in the hydraulic injection process, and can avoid incomplete fracturing phenomenon.

### 3.4.1 Experimental Set-Up

(i) Design of the inlet pipe seal pipe valve parts

To ensure the sealing effect, a set of injection pipe sealing pipe valve devices was designed (Fig. 3.24). The device is installed with two-way nut (1), positioning ferrule

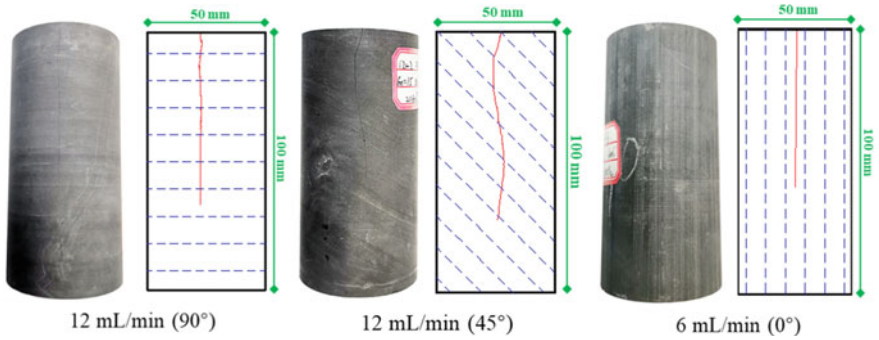


Fig. 3.23 Incomplete fracturing of specimens under condition of injecting water from sample end

(2), hexagonal hollow bolt (3) and incident steel pipe (4). The two-way nut, locating ferrule, hexagon hollow bolt and steel pipe are installed along the same axis. The assembly combination effect and principle are shown in Fig. 3.24.

The advantages of the device are shown as follows:

Positioning sleeve (2): the middle part of the outer wall is the arc wall, the diameter of the upper and lower edges of the positioning sleeve outer wall is less than the maximum diameter of the arc wall, and the part of the positioning sleeve outer wall near the two end is the inclined wall, the arc wall and the inner wall of the double pass nut (6) seal, to prevent the leakage of the injected fluid. By setting the outer wall of the positioning sleeve to the inclined wall and arc wall combination structure, in the positioning sleeve into the double nut and taking out from the double nut, so that the inclined wall to take out and put easier, the arc wall to ensure that the positioning sleeve and the double nut inner wall sealing, effectively avoid water through the outer

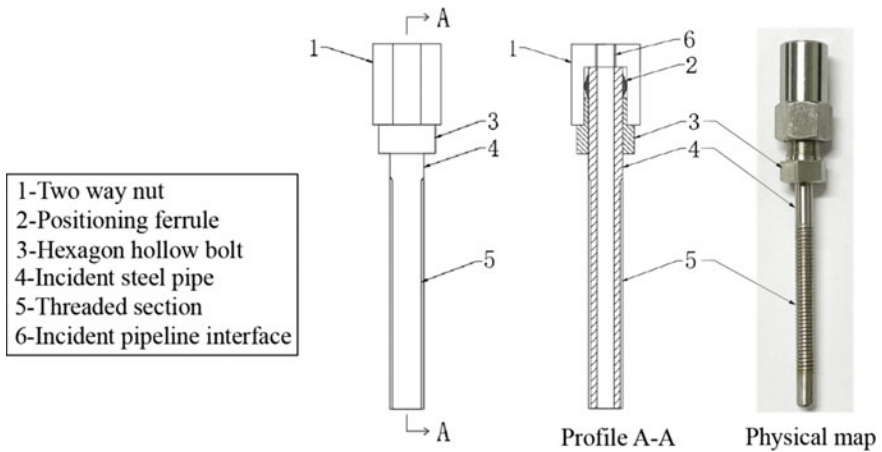


Fig. 3.24 Schematic diagram of sealing device of injection tube

wall along the incident steel pipe, greatly improve the sealing of the incident device. Injection steel pipe (4): the outer wall under the hexagonal hollow bolt with rough thread Sect. 3.5, the thread can effectively increase the contact area of the outer wall of the incident steel pipe and sealant, at the same time and increase the sealant and the incident steel pipe wall friction, avoid sealant sliding on the incident steel pipe wall, ensure the seal viscosity maximization, prevent liquid leakage along the wall, which can greatly improve the sealing effect of fluid injection. The smooth inner wall of the incident steel pipe can effectively reduce the resistance of the fluid when passing through the incident steel pipe, avoid the impact of the fluid fluctuations on the test results, reduce the load of the water pressure pump, and improve the stability of the device.

#### (ii) Sample preparation

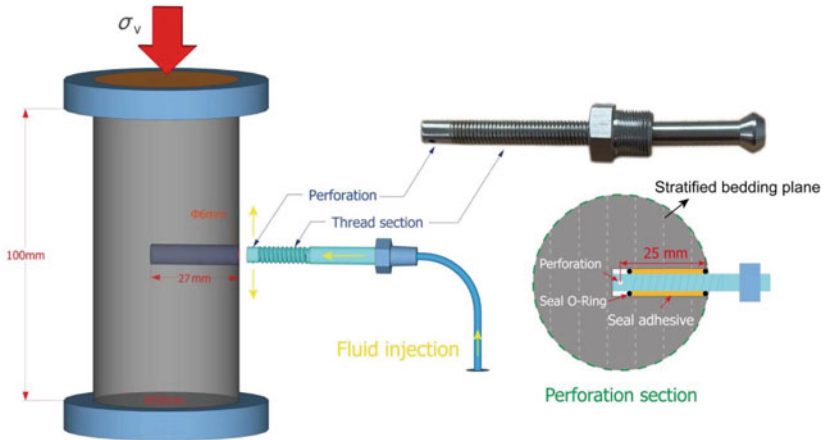
As shown in Fig. 3.25a, an injection hole ( $\Phi 6 \times 27$  mm) perpendicular to the specimen's longitudinal direction was drilled at the center of each cylindrical specimen. The specimens were shaped so that the orientations of bedding planes were aligned with the axial loading directions, causing the injection holes orthogonal to the bedding planes. Using epoxy AB adhesive, a 75-mm long 316 L steel tube with a sealed bottom and two perforations ( $\Phi 1$  mm) was fixed to the eyehole to simulate the wellbore, leaving an isolated, pressurized open hole section ( $\sim 4$  mm long) for fluid accumulation around the perforations, as depicted in Fig. 3.25b, c [27]. The specimens are then placed in a 260 °C oven for 24 h to achieve the optimal sealing effect.

#### (iii) Experiment apparatus

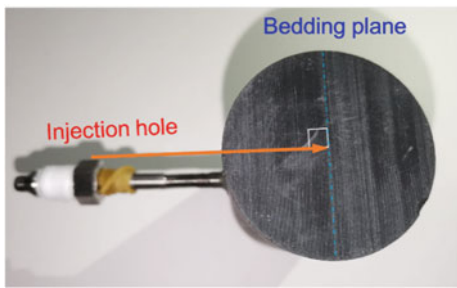
Laboratory experiments were conducted using a hydraulic fracturing system constituted by a TC-260L syringe pump and an axial loading device of the MTS 815 rock testing system. The syringe pump, manufactured by Jiangsu Tuochuang Scientific Research Instruments Co. Ltd., provides a total capacity of 266 mL, owns a maximum working pressure ( $P_{inj}$ ) of 100 MPa, and can adjust the fluid flow ( $V_{inj}$ ) from 0.01 to 120 mL/min. The injection mode of this pump can be maintained at either constant pressure or constant flow. Herein, the constant pressure injection mode was mainly adopted to initiate and sustain hydraulic fractures in shale specimens. Under this treatment, the fluid pressure is pumped stably by a constant pressure valve with feedback loop control (Fig. 3.26b), and the injection fluid will no longer maintain a constant flow rate but fluctuate with the fracture behavior [28, 29]. To capture real-time changes in pressure and flow rate during the fracturing process, we additionally installed pressure transducers and flow valves at the inlet of the wellbore, as shown in Fig. 3.26b [30].

#### (iv) Acoustic emission equipment

In the uniaxial hydraulic fracturing process, the Micro-Express Acoustic Emission detection system (hereinafter referred to as the AE system) developed by the American Physical Acoustic Corporation (PAC) is used to dynamically monitor the evolution law of fracture initiation and propagation in hydraulic fracturing. The AE monitoring system is mainly composed of three parts: PCI-Express 8 data acquisition



(a) 3D sample and perforation section view



(b) Relative position of injection tube and bedding plane

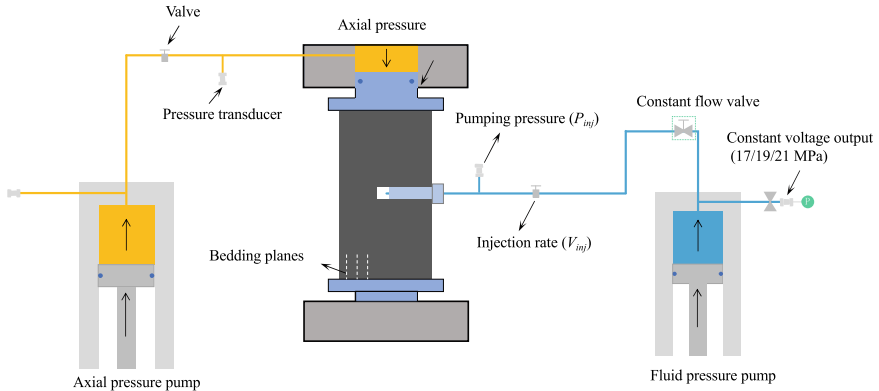


(c) Specimen assembly drawing

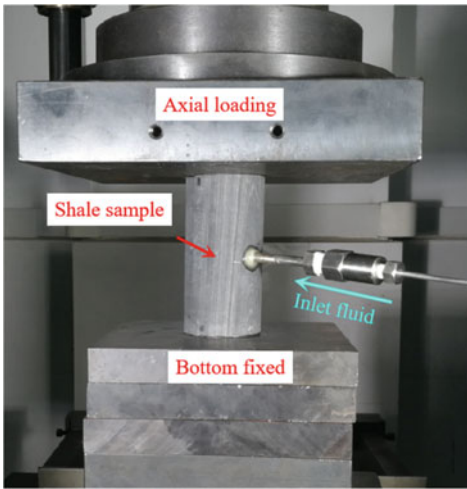
Fig. 3.25 Shale specimen preparation

system, NANO-30 AE probe and preamplifier. Each part is connected by a special data line to realize the dynamic acquisition, conversion and transmission of acoustic signals to electrical signals. A Acoustic emission characteristic parameters acquisition, waveform acquisition and analysis can be carried out at the same time. The AE acquisition system is equipped with an eight-channel AE graphics card, which can provide up to eight AE channels simultaneously to ensure that the sample fracture development process determines the real-time linear location, surface location, and spatial location and performs image display and storage simultaneously.

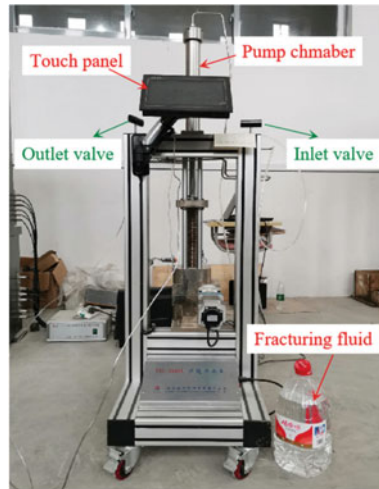
In this test, the AE system bandwidth is set as 1 kHz–1.2 MHz, the preset threshold value is 40 dB, the preamplifier is set as 40 dB, and other related acquisition parameters are shown in Table 3.8. Where, the system sampling frequency is 1 MSPS, representing 1 trillion samples being collected per second, equivalent to one sample being collected per microsecond. The PDT defines the peak time (Peak definition



(a) Schematic diagram of the test principle



(b) Axial pressure device



(c) TC-260 L injection pump

Fig. 3.26 Uniaxial hydraulic fracturing test system

time, in microseconds), and the setting of the PDT will affect the rise time and the peak amplitude of the identification signal peak. The HDT is the impact definition time (Hit definition time), and the HDT setting ensures that the AE signal detected in the structure is only a single impact when reflected into the system. HLT is the impact cloth layout time (Hit layout time), HLT avoids the non-true detection noise when the AE signal attenuation, and also improves the data acquisition speed.

Four NANO-30 probes were used in these tests to monitor the evolution of rock breakdown. As shown in Fig. 3.27, it is installed in four positions before and after the sample (mutual). Before installing the AE probe, apply agent to the probe end to ensure full contact with the specimen. After the probe is installed, the lead break

**Table 3.8** The acquisition parameter of AE system

Rate/MSPS	Signal threshold/dB	PDT/ $\mu$ s	HDT/ $\mu$ s	HLT/ $\mu$ s	Probe resonance frequency/kHZ
1 (1 MHz)	40 dB	200	800	1000	300

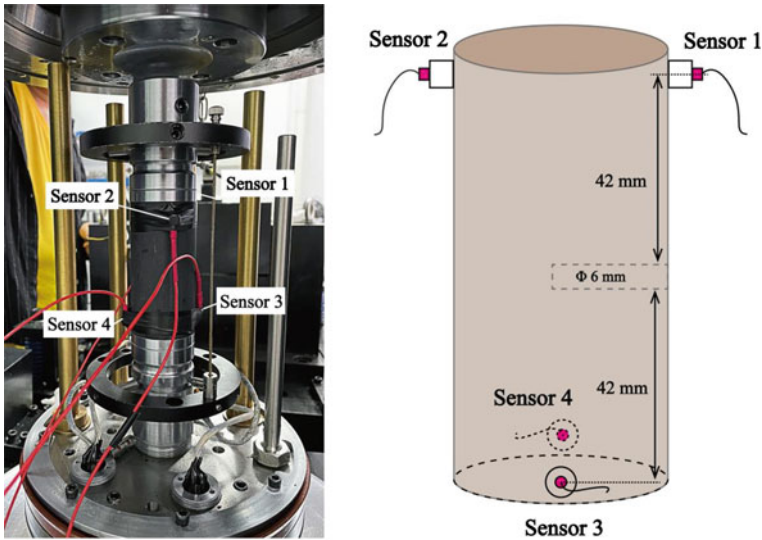


**Fig. 3.27** Schematic diagram of the layout of AE sensors

test is required to monitor the coupling quality of the probe and the sample and the positioning accuracy of the acoustic emission event. The specific operation method is to use a 0.5 mm HB automatic pencil with the test sample plane, and check the silent emission signal and the degree of consistency with the lead break position.

### 3.4.2 Experimental Procedures

Under the uniaxial stress state, the constant flow hydraulic fracturing test, the constant pressure hydraulic fracturing test and the shale anisotropic hydraulic fracturing test were conducted by changing pumping conditions and shale sample types. Constant flow hydraulic fracturing is to apply fluid pressure on the specimen at a constant injection rate (flow rate) until hydraulic fracturing occurs. Constant pressure hydraulic fracturing is the hydraulic fracturing of the sample due to static fatigue damage caused by constant fluid pressure acting on the sample [31]. In the anisotropic shale hydraulic fracturing test, the effect of shale bedding orientation (relative to the horizontal plane) is mainly considered when fracturing shale samples at a constant injection rate. In

this respect, the difference in fracturing effect between the conventional constant flow hydraulic fracturing test mainly depends on the initial axial stress, flow rate and bedding angle.

(i) Constant flow hydraulic fracturing test

Lin et al. [28] carried out a conventional triaxial hydraulic fracturing test using the Longmaxi shale, and analyzed the impact of in-situ stress difference and injection rate on the hydraulic fracturing effectiveness. However, there are few reports on the hydraulic fracturing effectiveness of Longmaxi shale without confining pressure. In order to compare the disturbance of the confining pressure on the breakdown pressure, circumferential deformation state and fracture propagation mode with reference to the test parameters of Lin et al. [28], the axial pressures of 5, 15 and 25 MPa were taken in turn to explore the impact of initial axial stress on hydraulic fracture effectiveness. At the same time, the injection rates of 6, 9 and 12 mL/min were selected to explore the disturbance effect of the injection rate of hydraulic fracturing. Meanwhile, test groups with incident conditions of 3 and 30 mL/min are added to further evaluate the change rule and evolution trend of fracture parameters at different injection rates. The specific test parameters are shown in Table 3.9.

(ii) Constant pressure hydraulic fracturing test

Based on the above specimens and apparatus, the specific experimental procedure is designed as follows: first, initial axial stress ( $\sigma_v$ ) is applied until the required experimental conditions are established at  $\sigma_v = 5$  MPa, which is approximately 5% of the uniaxial compression strength (UCS) of the selected shale. The reason for applying 5 MPa axial stress is to avert unintentional loading deviation of shale specimens during fluid injection and synchronously to make sure that no fractures are induced in the sample under this elastic compaction state. Then, the experiment commences when fracturing fluid (distilled water) is injected under the control of constant low and constant pressure modes, respectively; see Table 3.10. For convenience, the

**Table 3.9** Grouping parameters of hydraulic fracturing tests under constant flow injection conditions

No.	Sample	Bedding angle $\beta/^\circ$	Axial pressure $\sigma_1/\text{MPa}$	Injection rate $Q_{\text{inj}}/\text{mL/min}$
CI-90-3	Longmaxi shale	90	5	3
CI-90-6	Longmaxi shale	90	5	6
CI-90-12(CA-90-5)	Longmaxi shale	90	5	12
CI-90-18	Longmaxi shale	90	5	18
CI-90-30	Longmaxi shale	90	5	30
CA-90-15	Longmaxi shale	90	15	12
CA-90-25	Longmaxi shale	90	25	12
LV-90-12	Lushan shale	90	5	12

**Table 3.10** Grouping parameters of hydraulic fracturing tests under constant pressure injection condition

No.	Axial pressure $\sigma_1$ /MPa	Bedding plane $\beta/^\circ$	Injection rate $Q_{inj}$ /mL/min	Constant pressure $P_{con}$ /MPa	Remark
V-5	5	–	12	–	$P_b$
P-17	5	–	–	21	94% $P_b$
P-19	5	–	–	19	85% $P_b$
P-21	5	–	–	17	76% $P_b$
V-25	25	–	12	–	–

injection rate of the constant flow rate tests is fixed at 12 mL/min in line with Lin et al. [32] who performed flow-controlled triaxial hydraulic fracturing experiments using samples from the same shale formations. A constant flow test design (V-5) was first performed to attain the sample's instantaneous breakdown pressure ( $P_b = 22.35$  MPa) which serves as the upper limit for setting the subsequent output pressure reading on the constant pressure valve (i.e.,  $P_{con} = 17, 19,$  and  $21$  MPa). Additionally, another constant flow trial (V-25) was conducted under higher axial stress ( $\sigma_v = 25$  MPa), which is consistent with the axial restriction of a triaxial fracturing case ( $\sigma_v = 25$  MPa and  $\sigma_c = 20$  MPa) carried out by Lin et al. in the laboratory scale [32]. Through fracturing specimen V-25 and comparing its results to Lin et al. [32], we can appropriately evaluate and analyze the influence of the confining pressure on the breakdown pressure and the fracture morphology, with which the reliability of the uniaxial fracturing results under constant flow rate conditions can also be verified.

### (iii) Anisotropic Shale hydraulic fracture

The Longmaxi shale specimens with bedding angles of  $0^\circ$ ,  $45^\circ$ , and  $90^\circ$  (Fig. 3.28) were taken to conduct hydraulic fracture tests under a constant flow injection mode. Referring to Lin's test [28], the injection rate of 12 mL/min was also selected. In addition, due to the characteristics of the anisotropic difference caused by changes in the reservoir environment, constant flow fracturing tests were carried out for Lushan shale with  $0^\circ$ ,  $45^\circ$  and  $90^\circ$  bedding angles. The test parameters are shown in Table 3.11.

Based on the above test devices and methods (Figs. 3.24, 3.25 and 3.26) and the test parameters (Tables 3.9, 3.10 and 3.11), the uniaxial hydraulic fracture tests were conducted. The specific test steps are as follows:

- (1) Fracturing fluid: For better observation of the fracture geometry, a water-based fluorescent substance is added to the fracturing fluid before experiments. This substance can dissolve in water and hardly change the viscosity of the injected fluid. Under ultraviolet light, the mixed fracturing fluid shows bright yellow-green color, which will help identify whether fracturing fluid is leaking out during the fracturing process.
- (2) Sample installation and stress loading: Vaseline was spread evenly on the end face of the shale sample embedded incident tube and acoustic emission probe

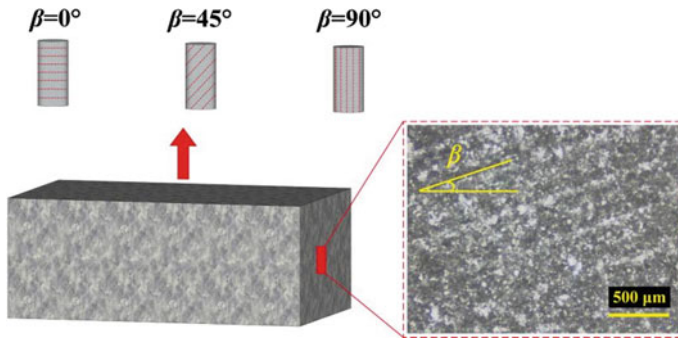


**Fig. 3.28** Schematic diagram of shale samples with anisotropic bedding planes

**Table 3.11** Grouping parameters of hydraulic fracturing tests adopting shale samples with anisotropic bedding planes

No.	Sample	Bedding angle $\beta/^\circ$	Axial pressure $\sigma_1/\text{MPa}$	Injection rate $Q_{\text{inj}}/\text{mL}/\text{min}$
CV-0-12	Longmaxi shale	0	5	12
CV-45-12	Longmaxi shale	45	5	12
CV-90-12	Longmaxi shale	90	5	12
LV-0-12	Lushan shale	0	5	12
LV-45-12	Lushan shale	45	5	12
LV-90-12	Lushan shale	90	5	12

to reduce friction. The stress control mode with a loading rate of 0.5 MPa/min was used to load the axial pressure to the target value, and the acoustic emission system started data acquisition simultaneously.

- (3) Fluid pressurization and fracturing: Before fluid injection, flow back into the pump pipeline for about 5 min to remove the possible residual air in the pipeline, and then connect the sample with the incident pipeline. Before starting the test, keep the constant voltage output mode of 0.5 MPa to check the pipeline for water leakage, then change the constant speed or keep the constant voltage mode, and set the preset constant current or constant voltage value. Acoustic emission accumulation time is recorded simultaneously with the fluid injection to distinguish the acoustic emission signals induced by fluid injection. The fluid pressure and the injection rate of the injection sample are measured by the pressure sensor ( $P_{\text{inj}}$ ) and the flow valve ( $V_{\text{inj}}$ ) near the wellhead, respectively, and the data is output in real-time by connecting to the computer. When a steep drop in fluid pressure or a steep increase in the injection rate is observed, hydraulic splitting damage occurred in the sample. After the sample breakdown, the injection continues for a period of time until the fluid pressure reaches balance and then the injection pump is turned off to ensure complete fracturing

of the sample. While closing the pump, the acoustic emission system and the axial pressure loading system to ensure the consistency of the data acquisition time scale;

- (4) Observation of fracture morphology: After experiments, microscope observation, industrial CT scanning (0.2 mm voxel resolution), and 3D laser scanning were jointly conducted to investigate fracture morphology characteristics under different injection modes. The high-definition LEICA M205A microscope enables us to obtain the microscopic details of the trajectory of hydraulic fractures on the surfaces of the fractured specimens. The CT scanning system (CD-130 BX/ $\mu$ CT, manufactured by Chongqing Zhence Science and Technology Co. Ltd.) has a maximum resolution of 0.005 mm and can accommodate a sample with a full size of 130 mm in diameter and 50 kg in weight, which is sufficient to identify whether there are hydraulic fractures induced in the shale specimens after the long duration pressurization. The 3D laser scanner was used to scan the fracture surface to visualize the extension distribution characteristics of the specimen in the 3Dimensional space.

### 3.4.3 Experiment Results and Analysis

- (i) Constant flow hydraulic fracturing

Unstable crack propagation leading to a macroscopic failure (a crack reaching the rock surface and splitting the specimen into two parts) is accompanied by a simultaneous drop of fluid pressure in the wellbore [33]. To quantitatively analyze the relationship between fluid pressure and crack propagation, we introduced a pressure decay rate ( $v_{\text{decay}}$ ) inside the wellbore following Gehne et al. [34], which can be expressed as

$$v_{\text{decay}} = \frac{P(t) - P(t + \Delta t)}{\Delta t} \quad (3.8)$$

where  $P(t)$  refers to the wellbore pressure at a certain time  $t$ , and  $\Delta t$  denotes an increment of time. According to Song et al. [35], Hu et al. [36], when ignoring the friction flow of fracturing fluid inside the wellbore, the wellbore pressure ( $P(t)$ ) can be considered the pumping (or wellhead) pressure ( $P_{\text{inj}}$ ) which is automatically monitored in real-time by a pressure transducer near the injection hole. Thus, Eq. (3.7) was rewritten as

$$v_{\text{decay}} = \frac{P_{\text{inj}}(t) - P_{\text{inj}}(t + \Delta t)}{\Delta t} \quad (3.9)$$

- (1) Typical curves of pumping pressure and injection rate versus time

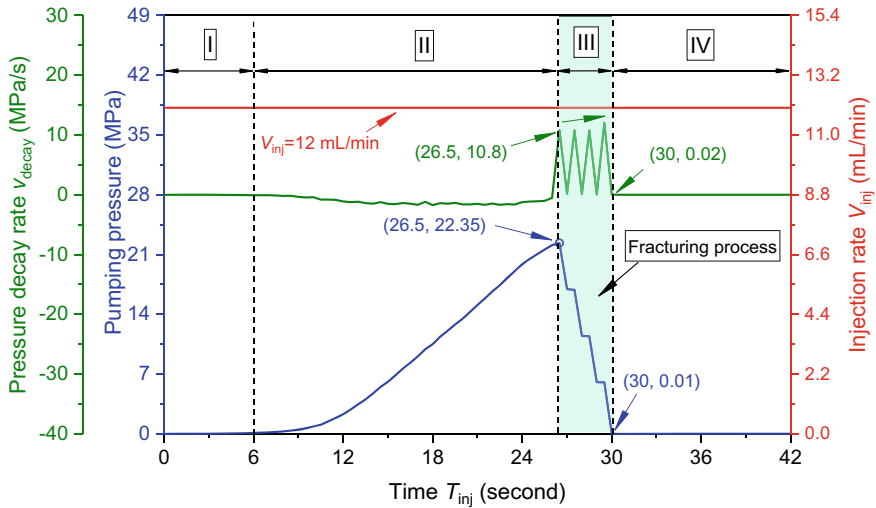


**Fig. 3.29** Curves of pumping pressure, injection rate, and pressure decay rate versus time

Similar to previous observations regarding conventional triaxial hydraulic fracturing [37, 38], in Fig. 3.29, the pumping pressure curves of the constant flow test (V-5) presented a trend of first increasing and then decreasing, which was characterized as four typical stages: initial pressurization stage (I), rapid pressurization stage (II), pressure drop stage (III) and post-peak stable pressure stage (IV).

## (2) Hydraulic fracture morphology

The fracture morphology of the specimen VC-5 surface before and after the test is shown in Fig. 3.30a–d. It is easy to see that there is no visible fracture on the sample surface before the test. After the pumping pressure reaches the breakdown pressure, the sample cracks and the fracture extends along the axial pressure direction as a whole. Once the specimen is completely cracked, the subsequently injected fluid will leak through the existing fractures (Fig. 3.30b). Figure 3.30d shows the 3D fracture morphology obtained by 3D laser scanning. The fracture surface is vertically straight and smooth, without bifurcation and convex surface, indicating that the sample has been completely broken. Figure 3.31 shows the microscopic fracture morphology of sample V-5. It can be seen that the hydraulic fracture morphology is not affected by its propagation direction. Even at the scale of 500  $\mu\text{m}$ , the hydraulic fracture is still straight and smooth, without branching and secondary fracture. The fracture width is evenly distributed along the length direction and is about 350  $\mu\text{m}$ .

### (ii) Disturbance of reservoir environment to hydraulic fracturing

According to the analysis of Sect. 3.2, the difference in the reservoir environment will directly affect the mineral composition and microstructure distribution of shale, and then affect the hydraulic fracturing and the fracture propagation law. To highlight

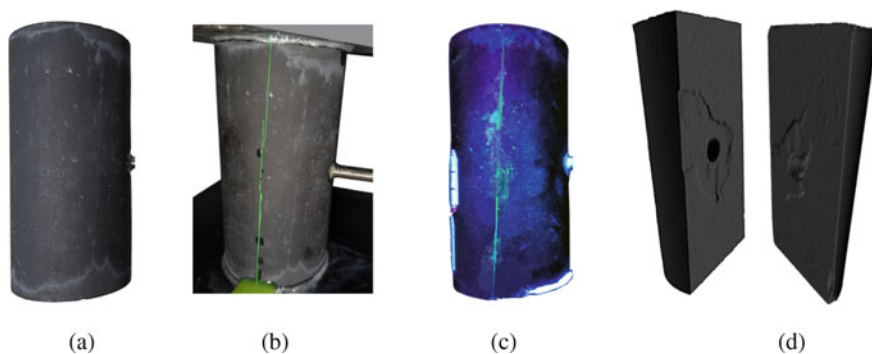


**Fig. 3.30** Fracture morphology of specimen VC-1 sourced from Longmaxi shale reservoirs **a** before experiment, **b** during experiment, **c** after experiment, **d** 3D view of fractured surface

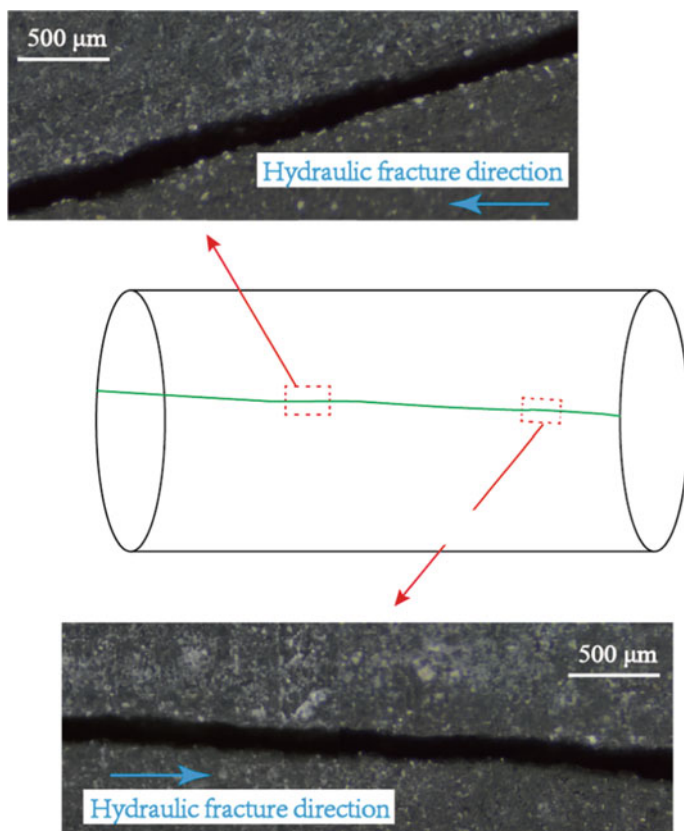


**Fig. 3.31** Micrograph showing some details of the hydraulic fracture morphology of specimen V-5

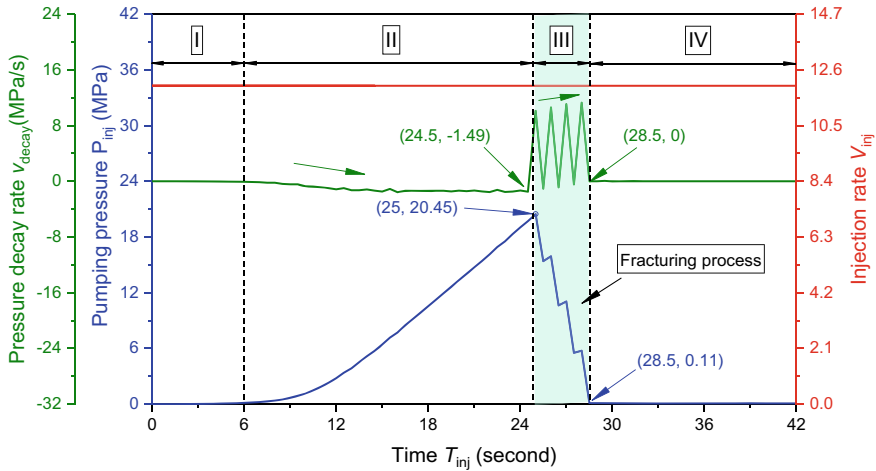


**Fig. 3.32** Curves of pumping pressure versus time of specimen LV-90-12 sourced in Lushan Mine

the unique characteristics of hydraulic fracturing of Longmaxi shale, a constant flow hydraulic fracturing test was also conducted for the Lushan shale samples. Here, the sample LV-90-12 is taken as an example, and its hydraulic fracturing is analyzed.

The pump pressure–time curve of the sample LV-90-12 is shown in Fig. 3.32. Overall, under the same axial pressure and injection rate conditions, the evolution trend of pump pressure, injection rate and pump pressure decay rate of Lushan shale in the hydraulic fracturing process is consistent with those of Longmaxi shale. However, compared with Longmaxi shale, the breakdown pressure, injection time and peak decay rate of Lushan shale are significantly reduced. This is because there are many primary defects such as pores and microcracks in the Lushan shale (see Sect. 3.2.3 of this chapter), which makes it easier to induce fracture initiation and propagation when constant flow pressurization occurs.

Figure 3.33 shows the hydraulic fracture morphology of Lushan shale. The hydraulic fractures of Longmaxi shale mainly propagate along the bedding plane, and the fracture surface is relatively smooth. Due to the influence of internal micro fractures and uneven distribution of clay minerals, the fracture surface of Lushan shale is relatively rough, and the concave-convex surface fluctuates significantly (Fig. 3.32).

To further analyze the disturbance of rock structure difference to the hydraulic fracture propagation law, the fracture morphology of Lushan shale was observed with a stereomicroscope at the same magnification (500  $\mu\text{m}$ ), and the results are shown in Fig. 3.34. Comparing Figs. 3.31 and 3.34, it can be found that although the hydraulic fracture of Lushan shale with significant heterogeneity propagates along the axial direction of the specimen, its opening decreases significantly and changes unevenly, making it difficult to observe the fracture morphology directly. Compared with the smooth and straight fracture morphology of Longmaxi shale, the main hydraulic fracture of Lushan shale branches into secondary fractures, and its fracture

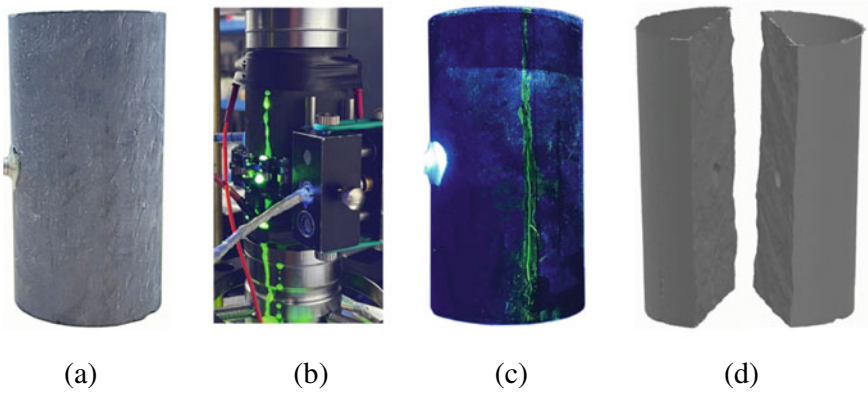


**Fig. 3.33** Surface fracture morphology of specimen LV-90-12 sourced in Lushan Mine. **a** Before experiment. **b** During experiment. **c** After experiment. **d** 3D view of fractured surface

morphology is tortuous and complex. This is because Lushan shale contains many micro defects and holes, which leads to the hydraulic fracture tends to crack along the direction of the weakest mechanical properties of the rock matrix, leading to the main fracture morphology becoming more tortuous.

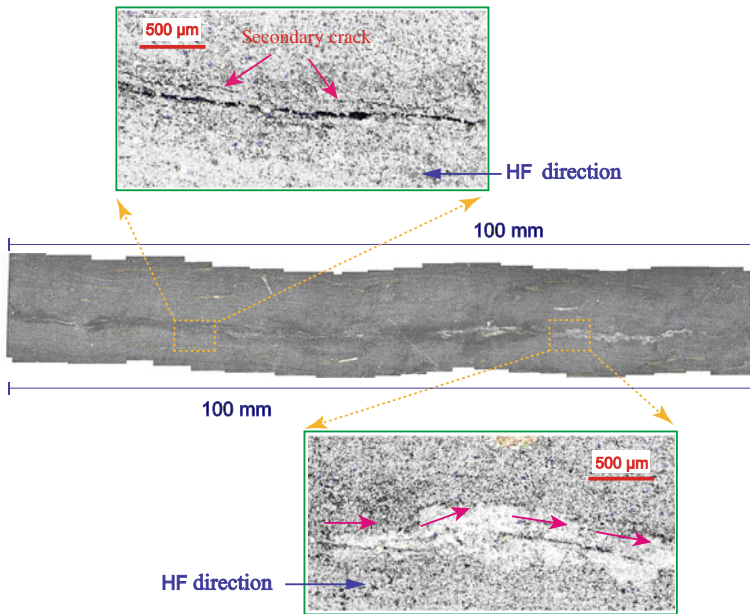


**Fig. 3.34** Microscopic fracture morphology of specimen LV-90-12 sourced in Lushan Mine

### 3.5 Characteristics of True Triaxial Hydraulic Fracture

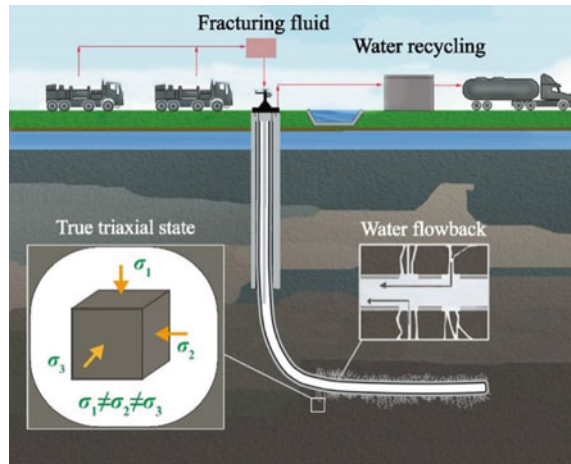
During the hydraulic fracturing construction process on the site, the deep rock bears the anisotropic and true triaxial pressure (Fig. 3.35). The physical model test of true triaxial hydraulic fracturing was carried out to simulate the pressure environment conditions of the underground rock. Three mutually perpendicular servo-hydraulic independent control flat jacks were applied to the sample's triaxial unequal pressure stress. In combination with the pump pressure–time curve, the rock fracture process was qualitatively analyzed, the expansion form of hydraulic fractures under true triaxial stress was described, and the morphological characteristics of the true triaxial hydraulic fracturing network were analyzed.

#### 3.5.1 Sample Preparation and Test Equipment

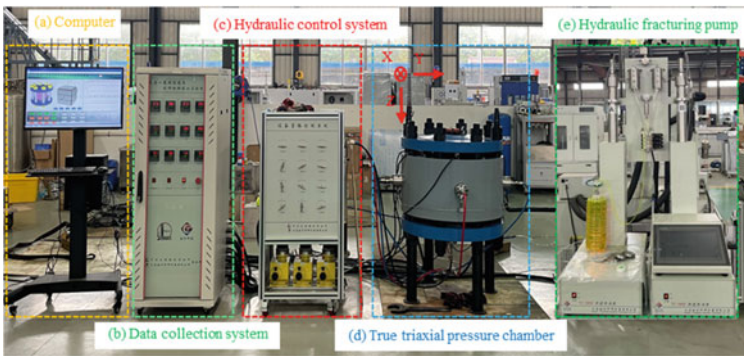
##### (i) True three-axis hydraulic fracking test system

Figure 3.36 shows the true triaxial hydraulic fracturing physical model testing machine and working diagram. The true three-axis hydraulic fracturing test system consists of three parts: the true three-axis loading system (including the true three-axis pressure chamber, the operating computer and the hydraulic control system), the pump pressure injection system (the hydraulic injection pump), and the data acquisition system. The true three-axis loading system adopts the servo motor control (power 400 W), which can realize the accurate servo control of displacement and pressure. The true three-axis pressure chamber cylinder block is made of high-strength 2507 duplex stainless steel, the pressure cavity roof is fixed, the other five sides

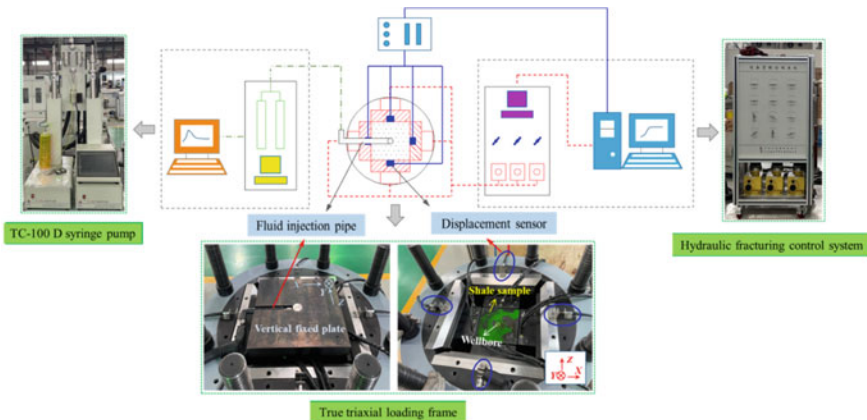
**Fig. 3.35** On-site true triaxial stress environment in situ reservoir



are equipped with hydraulic pistons (maximum stroke 10 mm), and the axial pressure shall be applied independently to the three directions of the sample XYZ. The true three-axis load system can output a maximum output pressure of 50 MPa, and a unique hydraulic mechanism is designed to recover the main hydraulic cylinder to facilitate the rapid removal of the sample. The pump pressure injection system is equipped with a model TC-100D injection pump. The pump is a double with cylinder layout, cylinder A discharging simultaneously as cylinder B suction to ensure continuous and constant flow rate without pulse liquid injection sample injection. Injection pumps can provide real-time monitoring of internal flow pressure and flow signal. The technical parameters are: the working pressure is 70 MPa, the flow adjustment range is 0.01–30 mL/min, the effective volume of the pump body is 100 mL, and the pressure accuracy is 0.1% FS.



(a) Hydraulic fracturing test system



(b) Schematic diagram of the hydraulic fracturing system

Fig. 3.36 True triaxial hydraulic fracturing test system

## (ii) Sample preparation

The rocks used in the test were taken from the outcrop shale reservoir of Longmaxi Formation, Sichuan Basin, as described in Sect. 3.2. Based on the allowable sample size of the test machine, bedding inclination, relative orientation of wellbore and bedding, fracture expansion path, mutual disturbance between seams, change of fluid pressure in the seam and the difficulty of sampling, transportation, loading and unloading. The length of the cubic sample specification used in the true three-axis hydraulic fracture are 400 mm [29], 300 mm [39], 200 mm [40], 100 mm [41] and 50 mm [42]. Considering the size of the confining pressure cavity and the difficulty of installation and disassembly, the specification is  $200 \times 200 \times 200$  mm shale test sample. Considering the size of the confining pressure chamber and the difficulty of installation and disassembly, the true triaxial hydraulic fracture shale sample carried out in this paper is  $200 \times 200 \times 200$  mm, taking into account the difference of bedding dip anisotropy ( $\beta = 0^\circ, 45^\circ$  and  $90^\circ$ ), the appearance of the sample is shown in Fig. 3.37. The sample appearance is shown in Fig. 3.37. The centre size of the sample is  $\Phi 25 \times 110$  mm round hole, with  $90^\circ, 45^\circ$  and  $0^\circ$  angles between drilling and shale bedding.

## (iii) Fracture design

In this test, the high-strength steel pipe with a length of 100, 15 mm outer diameter, and 10 mm internal diameter is used. The schematic diagram and physical objects are shown in Fig. 3.38. The ring groove of the steel pipe outer wall is 5 mm apart to increase the friction resistance of the steel pipe outer wall. Welding circular steel rings at the bottom near the outlet prevent colloidal infiltration and sealing of the outlet when filling the sealant.

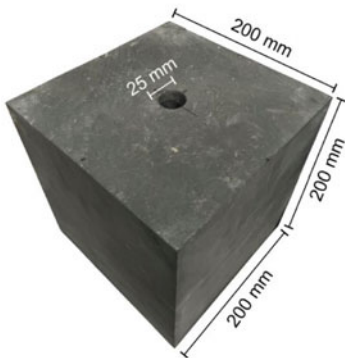


**Fig. 3.37** Shale specimen for triaxial hydraulic fracturing tests

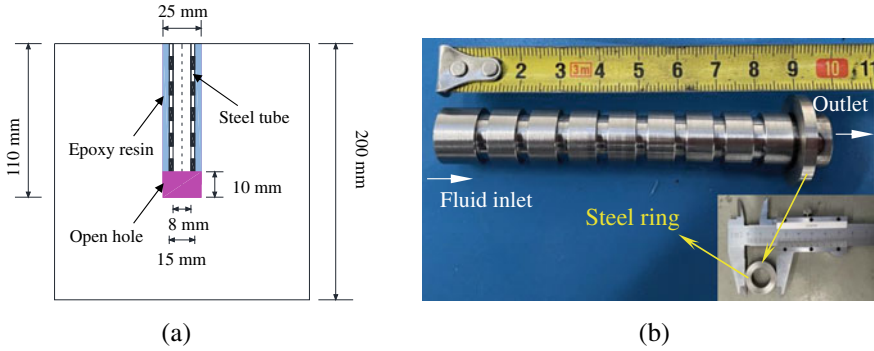
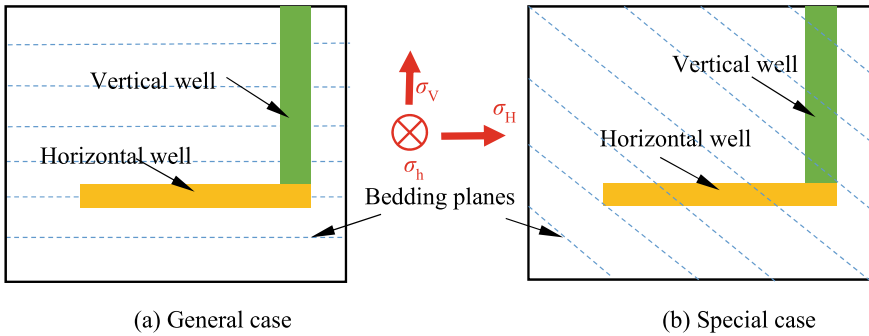


Fig. 3.38 Schematic diagram (a) and photographic image (b) of fracturing wellbore

### 3.5.2 Fracturing Scheme

Shale is a typical sedimentary rock, which forms a certain inclination angle level in the diagenesis stage. Due to the differences in the stress environment and diagenesis history, the direction of the shale reservoir level has prominent anisotropic characteristics. In this case, the bore will no longer be parallel or orthogonal to the group but at an angle  $\alpha$  to the bedding. To clarify the conventional horizontal well and vertical shaft wellbore layout of the traditional design ( $0^\circ$  or  $90^\circ$  Fig. 3.39a) and the wellbore and bedding surface into a specific inclination particular case ( $45^\circ$ , Fig. 3.39b) between the hydraulic fracturing effect difference, based on the different ground stress conditions and level direction, prepared six shale samples for hydraulic fracturing test. As shown in Table 3.12, BP refers to the natural bedding surface. Assuming that the ground stress ratio in the main direction of the sample is consistent with the Japanese Minami-Nagaoka natural gas field (max: med: min = 4:3:2 [43]), the test maximum, middle, and minimum principal stresses are 12, 9, and 6 MPa, respectively. This assumption scales the stress state of the in situ reservoir to a certain extent, which can prevent the direct use of the in situ stress to cause the original fracture due to the uneven stress difference in the loading process, which is conducive to reducing the disturbance of the preloading process to the subsequent hydraulic fracturing process. Reugelsdijk et al. [44] and Zhou et al. [45] also proposed similar assumed conditions and parameter arrangements in the true three-axis hydraulic fracturing simulation. The influence of the ground stress direction is mainly considered here (maximum, middle and minimum principal stress size fixed, principal stress difference  $\Delta\sigma = 3$  MPa), fixed flow  $Q_{inj} = 20$  mL/min injection, simulating the fracturing situation shown in Fig. 3.39.

To explore the fracturing mechanism of complex fracture networks and the hydraulic fracturing process of characteristic rock strata. The scheme and related parameters grouping are shown in Table 3.12 and Fig. 3.40. It should be noted that the vertical stress v directions of samples 5 # and 6 # in Table 3.12 are not aligned with the Y-axis direction in Fig. 3.40 but in the Z-axis direction. This is because



**Fig. 3.39** Schematic diagram of the intersecting relationship between the wellbore and the shale formations

**Table 3.12** Hydraulic fracturing schemes under true triaxial stress state

No.	$\sigma_v$ /MPa	$\sigma_H$ /MPa	$\sigma_h$ /MPa	Bedding angle (relative to the horizontal plane BP)/ $^\circ$	Type of shaft arrangement
1#	12 ( $\sigma_{max}$ )	9 ( $\sigma_{med}$ )	6 ( $\sigma_{min}$ )	0	Vertical wellbore
2#	9 ( $\sigma_{med}$ )	12 ( $\sigma_{max}$ )	6 ( $\sigma_{min}$ )	0	Vertical wellbore
3#	12 ( $\sigma_{max}$ )	9 ( $\sigma_{med}$ )	6 ( $\sigma_{min}$ )	45	Inclinde wellbore
4#	6 ( $\sigma_{min}$ )	12 ( $\sigma_{max}$ )	9 ( $\sigma_{med}$ )	45	Inclinde wellbore
5#	12 ( $\sigma_{max}$ )	9 ( $\sigma_{med}$ )	6 ( $\sigma_{min}$ )	90	Horizontal wellbore
6#	9 ( $\sigma_{med}$ )	12 ( $\sigma_{max}$ )	6 ( $\sigma_{min}$ )	90	Horizontal wellbore

only the top cap is movable in the true triaxial circumference pressure cavity. To realize the sample stress state during horizontal wellbore construction (the wellbore direction is consistent with the minimum ground stress direction), assume that the Z-axis direction is the direction of vertical stress applied here. Therefore, 5 # and 6 # samples simulate the positive fault stress state (normal-faulting stress regime) and tectonic stress state (tectonic stress regime), respectively, 3 # sample is the positive fault stress state, and 4 # sample is the reverse fault stress state (reverse faulting stress regime).

### 3.5.3 Analysis of Fracturing Results

(i) Analysis of pump pressure time curve

Taking 5# as an example, the change curve of the true three-axial hydraulic fracturing pump is analyzed. As can be seen from Fig. 3.41, under the true triaxial stress state,

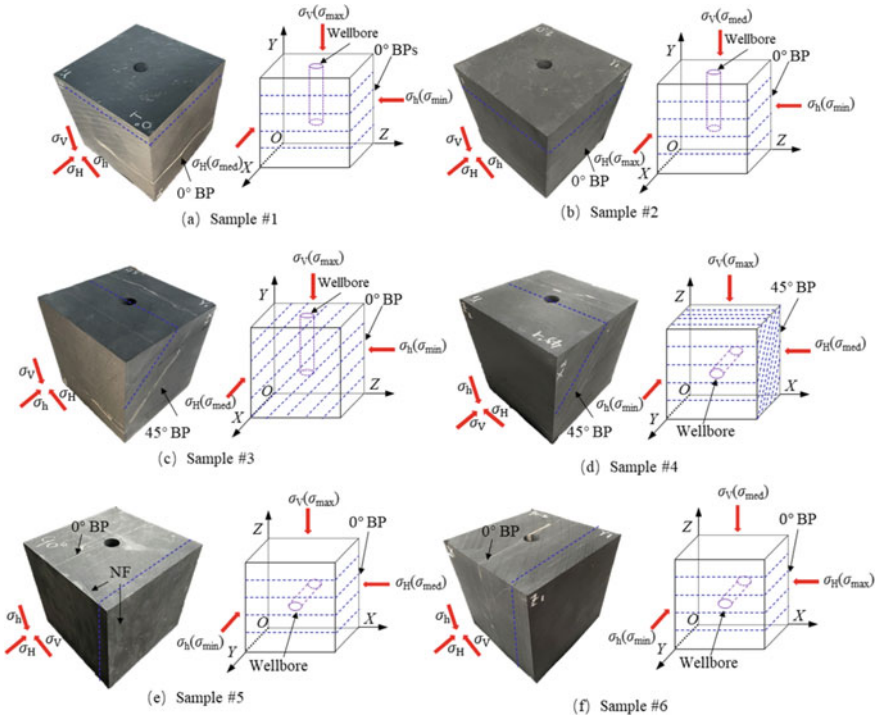
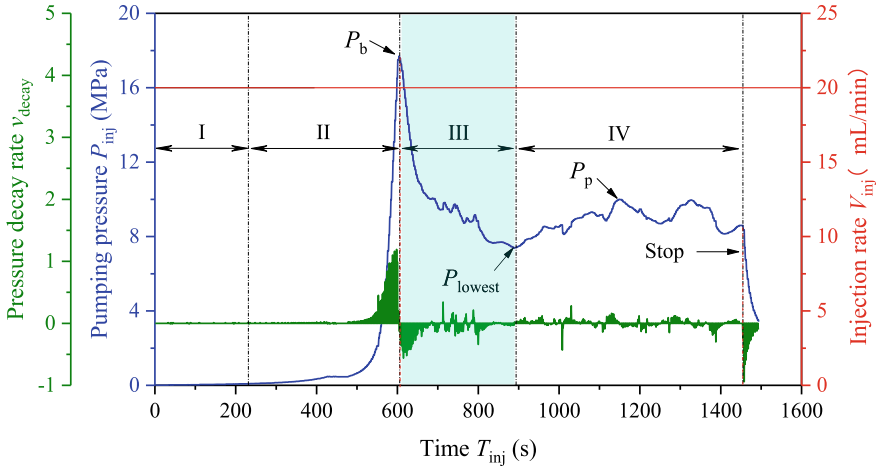


Fig. 3.40 Hydraulic fracturing test scheme of complex fracture network

the pump pressure–time curve is similar to the uniaxial state, which can still be divided into four stages: initial compression stage (I), rapid compression stage (II), post-peak pressure drops stage (III), and post-peak pressure stabilization stage (IV). The changing trend of the curve in the first three (I–III) phases and its corresponding physical processes are similar to the uniaxial stress state. In stage IV, the pump pressure curve does not steep to 0 as in the uniaxial state. This phenomenon is because, under the action of the lateral confining pressure, the hydraulic force induces the fracture to gradually close, and the newly injected fracturing fluid accumulates in the fracture, resulting in pressure to suppress, and the fluid pressure gradually increases. When the internal fluid pressure is greater than the fracture closure pressure, the fracture will be initiated, and the excess fluid will drive the hydraulic fracture to be further propagated. When a new fracture appears, the fluid pressure accumulated in the fracture is released and the pumping fluid pressure decreases. Therefore, in the process of unstable expansion, the pump pressure maintains the fluctuation state. This process corresponds to phase IV under the triaxial stress state. According to Fig. 3.41, the breakdown pressure  $P_b$  of the 5# sample is 17.69 MPa, and the lowest post-peak pump pressure ( $P_{lowest}$ ) is 8.79 MPa. The pressure suppression again causes the fracture starting pressure ( $P_p$ ) to be 10 MPa.



**Fig. 3.41** Pumping pressure curve versus time under true triaxial stress state

(ii) Morphological characterization of hydraulic fracture

Figure 3.42 shows the fracture form of the hydraulic fracturing end surface of shale samples in the true triaxial state. It can be seen that three approximately parallel extended hydraulic fractures ( $H_1$ ,  $H_2$ ,  $H_3$ , and  $H_4$ ) are induced near the wellbore, with the fracture direction consistent with the middle and principal stress  $\sigma_{med}$ . Different hydraulic fractures show different fracture expansion behavior when intersecting with the weakly cemented level ( $M_1$ ) and natural fracture ( $N_1$ ) in the rock. The closer distance of the hydraulic fracture  $H_1$  and  $H_2$  passes directly through the natural discontinuous surface  $M_1$  and  $N_1$ , and run through to the outer surface of the sample. In contrast, the hydraulic fracture  $H_3$  and  $H_4$  are directly overlapped with the natural discontinuous surface, and the fracturing fluid enters the activated natural fracture, resulting in a deflection in the extending direction of the hydraulic fracture mode. Engineering practice and physical simulation experimental data show that the intersection behaviors such as fracture crossing [46], slip, and branches are easy to disturb the expansion direction of hydraulic fracture, leading to complex fracture mesh patterns in the reservoir hydraulic fracturing process.

Shale reservoirs also differ due to different buried environments, rock properties, and stress conditions. Based on this background, this chapter takes the Longmaxi shale in Sichuan province as the primary research object and the Lushan shale as the comparison object. Studies of the mineral composition and microstructure of two types of shale have been carried on. Based on the plugging device independently designed by the author, the hydraulic fracturing test under the single axis and true three-axis stress state was conducted to explore the influence of the shale reservoir rock properties and stress conditions (single axis or true three-axis) on the reservoir rock fracture pressure and fracture expansion law.

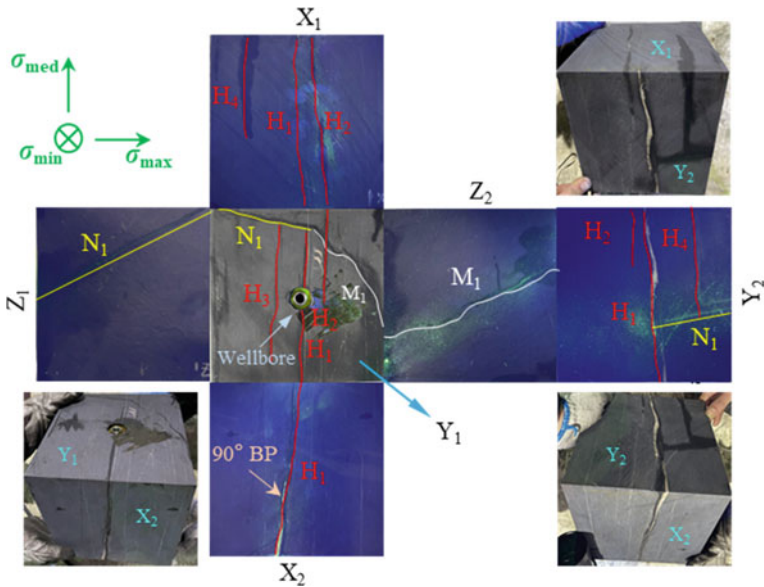


Fig. 3.42 Fracture propagation morphology of fractured specimens

## References

1. Ma XH, Xie J, Yong R, Zhu YQ (2020) Geological characteristics and high production control factors of shale gas reservoirs in Silurian Longmaxi formation, southern Sichuan Basin, SW China. *Petrol Explor Dev* 47(05):841–855
2. Si X, Wang Z, Wang W (2016) Study on the high performance water-based drilling fluid in Longmaxi shale gas formation. *Energy Chem Industr* 37(05):41–46
3. Li W (2015) Petrological characteristics and shale gas enrichment of organic matter-rich shale in Jiangxi province. China University of Mining and Technology Xuzhou
4. Zhang XJ (2020) Flow mechanism and productivity model for heat-gas-fluid-solid interactions on permeability enhancement in heterogeneous shale volume fracturing. Chinese doctoral dissertations full-text database. China University of Mining and Technology Xuzhou
5. Liu SX (2015) Research on microscopic characteristics of carboniferous shale reservoir in Eastern Qaidamu Basin. China University of Petroleum (East China)
6. Li A, Ding WL, Zhang GL, Zhang MG, Zhang ZX, Yan BZ, Zhou CX, Chen ZZ, Bai P (2016) Reservoir characteristics of marine shale in the Malong block of eastern Yunnan Province and comparison analysis. *Earth Sci Front* 23(02):176–189
7. Feng YX, Zhang Y, Zhang YW (2020) Physical properties of shale gas reservoir in Xinkailing formation of Northwestern Jiangxi. *Jiangxi Coal Sci Technol* 2020(03):1–3+7
8. Loucks RG, Reed RM, Ruppel SC, Hammes U (2012) Spectrum of pore types and networks in mudrocks and a descriptive classification for matrix-related mudrock pores. *Am Assoc Pet Geol Bull* 96(6):1071–1098. <https://doi.org/10.1306/08171111061>
9. He X, Wu J, Yong R, Zhao SX, Zhou XJ (2021) Accumulation conditions and key exploration and development technologies of marine shale gas field in Changning-Weiyuan block, Sichuan Basin. *Acta Petrolei Sinica* 42(02):259–272
10. Liu HY, Tian ZY, Liu B, Guo R, Shi KB (2019) Classification and prediction of giant thick strongly heterogeneous carbonate reservoirs in the Middle East area: a case study of Mid-Cretaceous Mishrif Formation in the W oilfield of Iraq. *Acta Petrolei Sinica* 40(06):677–691

11. Zeng FH, Zhang Q, Chen SY, Guo JC, Fan Y (2020) Dynamic characterization of microscopic pore structures of shale under the effect of hydration: a case study of Longmaxi formation shale in the Changning area of the Sichuan Basin. *Nat Gas Ind* 40(10):66–75
12. Zhang S, Liu HM, Wang YS, Zhang SP, Zhang KH (2019) Diagenetic event of Paleogene shale and its influence on development characteristics of shale pore space in Dongying Sag. *Petrol Geol Recov Efficiency* 26(01):109–118
13. Zhao LQ, Feng JW (2018) Interrelationship study between rock mechanical stratigraphy and structural fracture development. *J Shandong Univ Sci Technol (Nat Sci)* 37(01):35–46
14. Yao Y, Liu D, Che Y, Tang D, Tang S, Huang W (2010) Petrophysical characterization of coals by low-field nuclear magnetic resonance (NMR). *Fuel* 89(7):1371–1380. <https://doi.org/10.1016/j.fuel.2009.11.005>
15. Liu Z, Liu D, Cai Y, Yao Y, Pan Z, Zhou Y (2020) Application of nuclear magnetic resonance (NMR) in coalbed methane and shale reservoirs: a review. *Int J Coal Geol*
16. Èriks K, Lucio F, Andrew GW, Yong JRJ, Tim DWC (2021) Parallel nuclear magnetic resonance spectroscopy. *Nat Rev Methods Primers* 27
17. Liu JF, Skoczylas F, Talandier J, Pu H (2016) Dismantling of the EB experiment: experimental research on the retrieved GBM and bentonite blocks. *Nucl Eng Des* 300:297–307. <https://doi.org/10.1016/j.nucengdes.2016.01.023>
18. Liu JF, Ni HY, Pu H, Huang BX, Yao QL (2021) Test theory, method and device of gas permeability of porous media and the application. *Chin J Rock Mech Eng* 300:297–307
19. Wu ZS, Feng ZJ, Shi XD, Hui Z (2020) Study on permeability of granite under different confining pressures and its permeability sensitivity. *Min Res Dev* 40(10):46–50
20. Cai MF, He MC, Liu DY (2002) *Rock mechanics and engineering*. Science Press, Beijing
21. Yang T, Xu C, Wang BX, Zhang L, Liao GH (2007) The cohesive strength and the friction angle in rock-soil triaxial tests. *China Min Mag* 16(12):104–107
22. Tan J, Xie J, Li L, Lyu Q, Han J, Zhao Z (2020) Multifractal analysis of acoustic emissions during hydraulic fracturing experiments under uniaxial loading conditions: a niutitang shale example. *Geofluids*. <https://doi.org/10.1155/2020/8845292>
23. Wan XL, He JM, Zheng B (2017) Effect of bedding orientation on hydraulic fracture propagation in shale under uniaxial compression. *J Eng Geol* 25(01):88–94
24. Chitrala Y, Moreno C, Sondergeld C, Rai C (2011) Microseismic and microscopic analysis of laboratory induced hydraulic fractures. In: *Society of petroleum engineers—Canadian unconventional resources conference 2011, CURC 2011*
25. He J, Zhang Y, Li X, Wan X (2019) Experimental investigation on the fractures induced by hydraulic fracturing using freshwater and supercritical CO<sub>2</sub> in shale under uniaxial stress. *Rock Mech Rock Eng* 52(10):3585–3596. <https://doi.org/10.1007/s00603-019-01820-w>
26. Zhao Y, Zhang Y, Wang C, Liu Q (2022) Hydraulic fracturing characteristics and evaluation of fracturing effectiveness under different anisotropic angles and injection rates: an experimental investigation in absence of confining pressure. *J Nat Gas Sci Eng*. 97:104343. <https://doi.org/10.1016/j.jngse.2021.104343>
27. Li Q, Wu X, Zhai C, Hu Q, Ni G, Yan F, Xu J, Zhang Y (2021) Effect of frequency and flow rate of pulsating hydraulic fracturing on fracture evolution. *Zhongguo Kuangye Daxue Xuebao/J China Univ Min Technol* 50(06):1067–1076
28. Lin C, He J, Li X, Wan X, Zheng B (2017) An experimental investigation into the effects of the anisotropy of shale on hydraulic fracture propagation. *Rock Mech Rock Eng* 50(3):543–554. <https://doi.org/10.1007/s00603-016-1136-4>
29. Tan P, Jin Y, Han K, Zheng X, Hou B, Gao J, Chen M, Zhang Y (2017) Vertical propagation behavior of hydraulic fractures in coal measure strata based on true triaxial experiment. *J Pet Sci Eng* 158:398–407. <https://doi.org/10.1016/j.petrol.2017.08.076>
30. Jin W, Arson C (2020) Fluid-driven transition from damage to fracture in anisotropic porous media: a multi-scale XFEM approach. *Acta Geotech* 15:113–144. <https://doi.org/10.1007/s11440-019-00813-x>
31. Zhou JW (2019) Investigation into the initiation behavior of hydraulic fractures in a tight sandstone formation driven by abnormal borehole pressure. *China University of Petroleum, Beijing*

32. Lu G, Gordeliy E, Prioul R, Bungler A (2017) Modeling initiation and propagation of a hydraulic fracture under subcritical conditions. *Comput Methods Appl Mech Eng.* 318:61–91. <https://doi.org/10.1016/j.cma.2017.01.018>
33. Gunarathna G, da Silva BG (2019) Influence of the effective vertical stresses on hydraulic fracture initiation pressures in shale and engineered geothermal systems explorations. *Rock Mech Rock Eng* 52(11):4835–4853
34. Gehne S, Benson PM, Koor N, Dobson KJ, Enfeld M, Barber A (2019) Seismo-mechanical response of anisotropic rocks under hydraulic fracture conditions: new experimental insights. *J Geophys Res Solid Earth* 124(9):9562–79. <https://doi.org/10.1029/2019JB017342>
35. Song C, Lu Y, Tang H, Jia Y (2016) A method for hydrofracture propagation control based on nonuniform pore pressure field. *J Nat Gas Sci Eng* 33:287–95. <https://doi.org/10.1016/j.jngse.2016.05.029>
36. Hu Q, Liu L, Li Q, Wu Y, Wang X, Jiang Z et al (2020) Experimental investigation on crack competitive extension during hydraulic fracturing in coal measures strata. *Fuel* 2020. <https://doi.org/10.1016/j.fuel.2019.117003>
37. Michael A, Gupta I (2021) A comparative study of oriented perforating and fracture initiation in seven shale gas plays. *J Nat Gas Sci Eng* 88(4–5):103801
38. Fu Y (2019) The study on the rule of slick-water fracturing fluid flow in plugging of main fracture during the fracture of hydraulic fracturing. Xi'an Shiyou University
39. Guo T, Zhang S, Qu Z, Zhou T, Xiao Y, Gao J (2014) Experimental study of hydraulic fracturing for shale by stimulated reservoir volume. *Fuel* 128:373–380. <https://doi.org/10.1016/j.fuel.2014.03.029>
40. Zhang F, Ma G, Liu X et al (2018) Experimental analysis of multiple factors on hydraulic fracturing in coalbed methane reservoirs. *Plos One* 13(4)
41. Wu S, Li T, Ge H, Wang X, Li N, Zou Y (2019) Shear-tensile fractures in hydraulic fracturing network of layered shale. *J Pet Sci Eng* 183:106428. <https://doi.org/10.1016/j.petrol.2019.106428>
42. Minaeian V, Dewhurst DN, Rasouli V (2020) An investigation on failure behavior of a porous sandstone using single-stage and multi-stage true triaxial stress tests. *Rock Mech Rock Eng* 53(8):3543–3562
43. Sato K, Wright C, Ichikawa M (1999) Post-frac analyses indicating multiple fractures created in a volcanic formation. *SPE Prod Facil* 14(4):61–63
44. Beugelsdijk LJJ, Pater C, Sato K (2000) Experimental hydraulic fracture propagation in a multi-fractured medium. In: *SPE Asia pacific conference on integrated modelling for asset management*
45. Zhou J, Chen M, Yan J et al (2008) Analysis of fracture propagation behavior and fracture geometry using a tri-axial fracturing system in naturally fractured reservoirs. *Int J Rock Mech Min Sci* 45(7):1143–1152
46. Fisher K, Warpinski N (2012) Hydraulic-fracture-height growth: real data. *SPE Prod Oper* 27(1):8–19

**Open Access** This chapter is licensed under the terms of the Creative Commons Attribution 4.0 International License (<http://creativecommons.org/licenses/by/4.0/>), which permits use, sharing, adaptation, distribution and reproduction in any medium or format, as long as you give appropriate credit to the original author(s) and the source, provide a link to the Creative Commons license and indicate if changes were made.

The images or other third party material in this chapter are included in the chapter's Creative Commons license, unless indicated otherwise in a credit line to the material. If material is not included in the chapter's Creative Commons license and your intended use is not permitted by statutory regulation or exceeds the permitted use, you will need to obtain permission directly from the copyright holder.

